The High-Resolution, Three-Dimensional Solution Structure of Human Interleukin-4 Determined by Multidimensional Heteronuclear Magnetic Resonance Spectroscopy[†,‡]

Robert Powers,[§] Daniel S. Garrett,[§] Carl J. March,[||] Eric A. Frieden,[||] Angela M. Gronenborn,*,[§] and G. Marius Clore*,[§]

Laboratory of Chemical Physics, National Institutes of Diabetes and Digestive and Kidney Diseases, National Institutes of Health, Building 2, Bethesda, Maryland 20892, and Immunex Corporation, 51 University Street, Seattle, Washington 98101

Received February 2, 1993; Revised Manuscript Received April 2, 1993

ABSTRACT: The high-resolution three-dimensional solution structure of recombinant human interleukin-4 (IL-4), a protein of ~15 kDa which plays a key role in the regulation of B and T lymphocytes, has been determined using three- and four-dimensional heteronuclear NMR spectroscopy. The structure is based on a total of 2973 experimental NMR restraints, comprising 2515 approximate interproton distance restraints, 102 distance restraints for 51 backbone hydrogen bonds, and 356 torsion angle restraints. A total of 30 structures was calculated by means of hybrid distance geometry–simulated annealing, and the atomic rms distribution about the mean coordinate positions for residues 8–129 is 0.44 ± 0.03 Å for the backbone atoms, 0.83 ± 0.03 Å for all atoms, and 0.51 ± 0.04 Å for all atoms excluding disordered side chains. The N- and C-terminal residues (1–7 and 130–133, respectively) appear to be disordered. The structure of IL-4 is dominated by a left-handed four-helix bundle with an unusual topology comprising two overhand connections. The linker elements between the helices are formed by either long loops, small helical turns, or short strands. The latter include a mini anti-parallel β-sheet. A best fit superposition of the NMR structure of IL-4 with the 2.25 Å resolution crystal structure [Wlodawer, A., Pavlovsky, A., & Gutschina, A. (1992) *FEBS Lett.* 309, 59–64] yields a backbone atomic rms difference of 1.37 Å which can be mainly attributed to tighter packing of the helices in the crystal structure. This is indicated by an approximately 20% reduction in the axial separation of three pairs of helices (α_A–α_C, α_A–α_D, and α_C–α_D) in the crystal structure relative to the NMR structure and may reflect the greater flexibility of the molecule in solution which is reduced in the crystal due to intermolecular contacts. Comparison of the NMR structure of IL-4 with the X-ray structures of two other related proteins, granulocyte–macrophage colony stimulating factor [Diedrichs, K., Boone, T., & Karplus, P. A. (1992) *Science 254*, 1779–1782] and human growth hormone [de Vos, A. M., Ultsch, M., & Kossiakoff, A. A. (1992) *Science 255*, 306–312], that bind to the same hematopoietic superfamily of cell surface receptors reveals a remarkably similar topological fold, despite the absence of any significant overall sequence identity, and substantial differences in the relative lengths of the helices, the lengths and the nature of the various connecting elements, and the pattern and number of disulfide bridges. Indeed, the C^α atom coordinates of 72 and 79 residues of IL-4 can be superimposed on the C^α coordinates of granulocyte–macrophage colony stimulating factor and human growth hormone with rms differences of ~1.7 and 2.0 Å, respectively.

Interleukin-4 (IL-4)[1] is a member of the cytokine family of proteins and plays a key role in the immune and inflammatory systems [see Paul and Ohara (1987), Yokota et al. (1988), Finkelman et al. (1990), Paul (1991), and Boulay and Paul (1992) for reviews]. IL-4 regulates B-cell proliferation and differentiation, modulates the survival, proliferation, and differentiation of T-cells, acts as a growth factor on mast cells, regulates macrophage activation, and induces the expression of VCAM-1 on endothelial cells. IL-4 is a potent inducer of human cytotoxic CD8+ T-cells, an activity which has been shown to be responsible for establishing tumor-specific systemic immunity to an established renal cancer by injection of renal tumor cells genetically engineered to secrete large doses of IL-4 locally (Golumbek et al., 1991). The very potent antitumor activity of IL-4 at the primary tumor site is also associated with the elicitation of a localized inflammatory infiltrate, dominated by eosinophils (Tepper et al., 1989, 1992). Additionally, IL-4 induces the expression of class I and II MHC molecules and the IgE low-affinity receptor

[1] Abbreviations: IL-4, human recombinant interleukin-4 (the numbering scheme used in the present article includes the four-residue sequence Glu-Ala-Glu-Ala at the N-terminus of the recombinant protein which is not part of the natural human IL-4; the natural sequence therefore starts at residue 5); NMR, nuclear magnetic resonance; Ig, immunoglobulin; HGH, human growth hormone; GM-CSF, granulocyte–macrophage colony stimulating factor; NOE, nuclear Overhauser effect; NOESY, nuclear Overhauser enhancement spectroscopy; ROE, rotating frame Overhauser effect; ROESY, rotating frame Overhauser enhancement spectroscopy; HOHAHA, homonuclear Hartmann–Hahn spectroscopy; HMQC, heteronuclear multiple quantum coherence; CT, constant time; HCACO, $C^\alpha H$ proton to α-carbon to carbonyl carbon correlation; HNHB, amide proton to nitrogen to $C^\beta H$ proton correlation; HN(CO)HB, amide proton to nitrogen to $C^\beta H$ proton (via carbonyl carbon); 3D, three-dimensional; 4D, four-dimensional; TPPI, time-proportional phase incrementation; SA, simulated annealing; rms, root mean square.

on resting B-cells. IL-4 causes immunoglobulin class switching of activated B-cells to IgE and IgG1, thereby generating and sustaining in vivo IgE responses and ensuring the dominance of IgG1 in a T-cell-dependent immune response (Kühn et al., 1991).

To further understand the structure–function relationship of IL-4 and its mode of interaction with its receptor, we have set out to elucidate the high-resolution, three-dimensional structure of IL-4 in solution by NMR spectroscopy. Recently, we presented the complete ^{1}H, ^{15}N, and ^{13}C resonance assignments of IL-4 (Powers et al., 1992a), the elucidation of its secondary structure (Garrett et al., 1992), and the determination of a low-resolution (second generation) tertiary structure (Powers et al., 1992b). At the same time, another low-resolution NMR structure was published by Smith et al. (1992). In this article, the focus is extended to the determination of a high-resolution three-dimensional structure of IL-4 using three- and four-dimensional heteronuclear NMR spectroscopy. The resulting fourth generation (Clore & Gronenborn, 1991a,b) structure is based on 2973 experimental NMR restraints, and the atomic rms distribution about the mean coordinate positions (excluding residues 1–7 and 130–133 at the N- and C-termini, which are disordered) is 0.44 ± 0.03 Å for the backbone atoms, 0.83 ± 0.03 Å for all atoms, and 0.51 ± 0.04 Å for all atoms excluding disordered side chains. This represents an approximate doubling in the number of experimental NMR restraints and an increase by a factor of more than 2 in the precision and accuracy of the coordinates relative to the previous NMR structure determinations of IL-4 (Powers et al., 1992b; Smith et al., 1992).

EXPERIMENTAL PROCEDURES

Sample Preparation. Uniformly (>95%) ^{15}N- and ^{15}N/^{13}C-labeled human recombinant IL-4 was expressed in yeast and purified as described previously (Powers et al., 1992a). The version of recombinant IL-4 used comprises the tetrapeptide sequence Glu-Ala-Glu-Ala added to the N-terminus of the natural sequence. In the present article, residues are numbered from the N-terminal Glu as residue 1, so that the natural IL-4 sequence starts at residue 5. In addition, the two potential N-linked glycosylation sites at Asn 42 and Asn 109 in the natural sequence were changed to Asp by site-directed mutagenesis to prevent hyperglycosylation in the yeast host (Curtis et al., 1991). Samples for NMR contained 2 mM ^{15}N- or ^{13}C/^{15}N-labeled IL-4, pH 5.7, dissolved in either 90% H_2O/10% D_2O or 99.996% D_2O.

NMR Spectroscopy. All spectra reported were recorded at 36 °C on Bruker AMX600 and AM600 spectrometers equipped with a triple-resonance ^{1}H/^{13}C/^{15}N probe. Quadrature detection in the indirectly detected dimensions was obtained using the TPPI–States method (Marion et al., 1989a). For spectra recorded in H_2O, water suppression was achieved by the use of spin–lock pulses to randomize magnetization of protons not attached to ^{15}N (Messerle et al., 1989). In the case of the 4D ^{13}C/^{13}C-edited NOESY spectrum, suppression of undesired coherence transfer pathways was achieved by means of pulse field gradients (Bax & Pochapsky, 1992), enabling a minimal two-step phase cycle to be employed (Vuister et al., 1993).

The present structure is based on the following series of spectra: 2D HMQC-J (Kay & Bax, 1990; Forman-Kay et al., 1990), 3D ^{15}N- (Marion et al., 1989b; Zuiderweg & Fesik, 1989) and ^{13}C-edited NOESY (Ikura et al., 1990a; Zuiderweg et al., 1990), 3D ^{1}H–^{15}N HMQC-NOE-HMQC (Ikura et al., 1990b), 3D ^{15}N- (Clore et al., 1990a) and ^{13}C-edited ROESY (Clore et al., 1991a), 3D ^{15}N-edited HOHAHA (Marion et

al., 1989b; Clore et al., 1991a), 3D HN(CO)HB (Grzesiek et al., 1992), 3D HNHB (Archer et al., 1991), 3D long-range ^{13}C–^{13}C correlation (Bax et al., 1992), 3D coupled CT-HCACO (Powers et al., 1991; Vuister et al., 1992), and 4D ^{15}N/^{13}C- (Kay et al., 1990) and ^{13}C/^{13}C-edited NOESY (Clore et al., 1991b; Zuiderweg et al., 1991; Vuister et al., 1993). Examples of the quality of spectra not shown here are found in previous publications, together with details of their experimental implementation: see Garrett et al. (1992) and Powers et al. (1992a,b). Experimental details regarding spectra not reported in these publications are provided below.

The 4D ^{13}C/^{13}C-edited NOESY spectrum was recorded with 2 scans per increment and a total measuring time of 84 h using sine bell shaped pulse field gradients (of strength 7 G/cm at their maximum) applied along the z axis. The pulse scheme and experimental setup employed were exactly as described by Vuister et al. (1993). The 4D ^{15}N/^{13}C-edited NOESY spectrum was recorded with 4 scans per increment and a total measuring time of 6 days using the pulse scheme described by Kay et al. (1990). Because this experiment includes a double ^{15}N/^{13}C heteronuclear filter which is highly efficient at eliminating any potential artifacts arising from undesired coherence transfer pathways, no pulse field gradients were employed.

The spectral widths for the 3D long-range ^{13}C–^{13}C correlation experiment in the indirectly detected ^{13}C dimensions were 87.196 ppm for F_1 and 3.657 ppm for F_2 with the carrier at 30 ppm, and the spectral width in the ^{1}H acquisition dimension was 8.011 ppm with the carrier at 2.67 ppm. The spectral widths for the coupled 3D CT-HCACO experiment in the indirectly detected ^{13}C dimensions were 12.05 ppm for F_1(^{13}CO) and 33.13 ppm for F_2(^{13}C$^\alpha$) with the carrier at 176.68 ppm for F_1 and 56 ppm for F_2, and the spectral width in the ^{1}H acquisition dimension was 4.17 ppm with the carrier at 4.67 ppm. The spectral widths for the 4D ^{13}C/^{13}C-edited NOESY, 3D ^{13}C-edited ROESY, 4D ^{15}N/^{13}C-edited NOESY, and the 3D ^{15}N-edited ROESY NMR experiments in the indirectly detected ^{15}N and/or ^{13}C dimensions were 30.01 and 20.71 ppm, respectively, with the carrier at 115 and 63.71 ppm, respectively. For the 3D ^{13}C-edited ROESY experiment, the spectral width in the indirectly detected ^{1}H dimension was 9.26 ppm with the carrier at 3 ppm, and the spectral width in the acquisition dimension was 19.84 ppm with the carrier at 8.21 ppm. For the 3D ^{15}N-edited ROESY experiment, the spectral width in the indirectly detected ^{1}H dimension was 11.41 ppm with the carrier at 4.67 ppm, and the spectral width in the ^{1}H acquisition dimension was 13.44 ppm with the carrier at 4.67 ppm. For the 4D ^{13}C/^{15}N-edited NOESY experiment, the spectral width in the indirectly detected ^{1}H dimension was 11.41 ppm with the carrier at 4.67 ppm, and the spectral width in the ^{1}H acquisition dimension was 10.04 ppm with the carrier at 4.67 ppm. For the 4D ^{13}C/^{13}C-edited NOESY experiment, the spectral width in the indirectly detected ^{1}H dimension was 8.96 ppm with the carrier at 3.98 ppm, and the spectral width in the ^{1}H acquisition dimension was 10.04 ppm with the carrier at 4.67 ppm.

For the 3D long-range ^{13}C–^{13}C correlation experiment, the number of points acquired in the various dimensions was 128 complex points in F_1(^{13}C), 16 complex points in F_2(^{13}C), and 256 complex points in F_3(^{1}H). For the coupled 3D CT-HCACO experiment, the number of points acquired in the various dimensions was 64 complex points in F_1(^{13}CO), 32 complex points in F_2(^{13}C$^\alpha$), and 256 complex points in F_3-(^{1}H). For the 3D ^{13}C- and ^{15}N-edited ROESY experiments, the number of points acquired in the various dimensions was

128 complex points in $F_1(^1H)$, 32 complex points in $F_2(^{13}C$ or $^{15}N)$, and 512 complex points in $F_3(^1H)$. For the 4D $^{13}C/^{15}N$-edited NOESY experiment, the number of points acquired in the various dimensions was 16 complex points in $F_1(^{15}N)$, 64 complex points in $F_2(^1H)$, 16 complex points in $F_3(^{13}C)$, and 256 complex points in $F_4(^1H)$. For the 4D $^{13}C/^{13}C$-edited NOESY experiment, the number of points acquired in the various dimensions was 18 complex points in $F_1(^{13}C)$, 64 complex points in $F_2(^1H)$, 16 complex points in $F_3(^{13}C)$, and 300 complex points in $F_4(^1H)$. One zero-filling was used in all dimensions, and in the case of the 4D $^{13}C/^{13}C$-edited NOESY and the 4D $^{13}C/^{15}N$-edited NOESY experiment, linear prediction by means of the mirror image technique (Zhu & Bax, 1990) was used with zero-filling to further extend the data in the $F_1(^{13}C)$ and $F_3(^{15}N$ or $^{13}C)$ dimensions.

All spectra were processed on a Sun Sparc Workstation using in-house routines for Fourier transformation (Kay et al., 1989; G. Vuister, unpublished) and linear prediction (Zhu & Bax, 1990), together with the commercially available software package NMRZ (New Methods Research, Inc., Syracuse, NY) for the processing of 2D planes. Analysis of the 3D and 4D spectra was carried out using the in-house programs PIPP and STAPP (Garrett et al., 1991; D. S. Garrett, unpublished).

The mixing times employed for the heteronuclear-edited NOESY and ROESY experiments were as follows: 120 ms for the 3D ^{13}C- and ^{15}N- edited NOESY experiments; 150 ms for the 3D $^1H-^{15}N$ HMQC-NOE-HMQC experiment; 110 and 107 ms for the 4D $^{15}N/^{13}C$- and $^{13}C/^{13}C$-edited NOESY experiments, respectively; and 35 and 40 ms for the ^{15}N- and ^{13}C-edited ROESY experiments, respectively.

Interproton Distance Restraints. NOEs were assigned from 3D and 4D heteronuclear-edited NOESY spectra recorded with mixing times ranging from 100 to 150 ms. The NOEs were classified into strong, medium, and weak corresponding to interproton distance restraints of 1.8–2.7 Å (1.8–2.9 for NOEs involving NH protons), 1.8–3.3 Å (1.8–3.5 for NOEs involving NH protons), and 1.8–5.0 Å, respectively (Williamson et al., 1985; Clore et al., 1986). Thus, the lower bounds for the interproton distance restraints were set to the sum of the van der Waals radii of two protons. Upper distance limits for distances involving methyl protons and non-stereospecifically assigned methylene protons were corrected appropriately for center averaging (Wüthrich et al., 1983), and an additional 0.5 Å was added to the upper distance limits for NOEs involving methyl protons (Clore et al., 1987; Wagner et al., 1987).

Torsion Angle Restraints and Stereospecific Assignments. ϕ, ψ, and χ_1 torsion angle restraints and stereospecific assignments of β-methylene protons were derived from the following data. Approximate intraresidue and sequential interproton distance restraints involving the NH, $C^\alpha H$, and $C^\beta H$ protons were obtained from ROE data to avoid complications arising from spin diffusion (Bothner-By et al., 1984; Bax & Davis, 1985; Bax et al., 1986) using 3D ^{13}C-edited ROESY (40 ms mixing time; Clore et al., 1991a) and 3D ^{15}N-edited ROESY (35 ms mixing time; Clore et al., 1990a) experiments. 3D ^{15}N-edited HOHAHA (44.6 ms mixing time), HNHB, and HN(CO)HB experiments were used to obtain a qualitative estimate of the magnitude of the $^3J_{\alpha\beta}$, $^3J_{N-H\beta}$, and $^3J_{CO-H\beta}$ coupling constants, respectively (Clore et al., 1991a; Archer et al., 1991; Grzesiek et al., 1992). Finally, $^3J_{HN\alpha}$ coupling constants were obtained from an HMQC-J spectrum (Kay & Bax, 1989), as described by Forman-Kay et al. (1990).

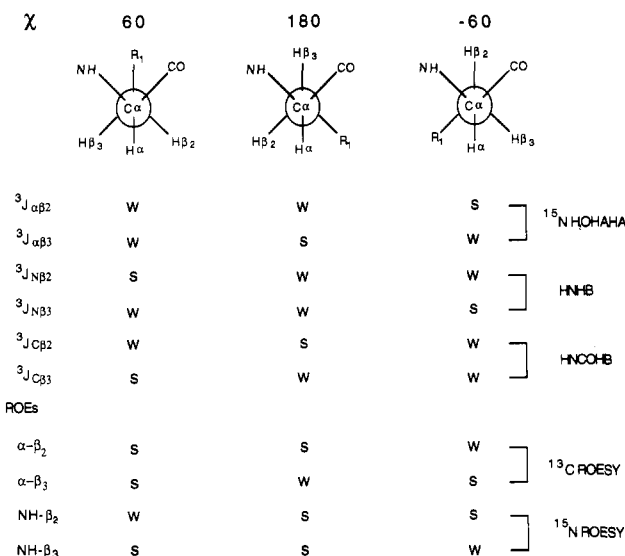| χ	60	180	-60	
$^3J_{\alpha\beta2}$	W	W	S	^{15}N HOHAHA
$^3J_{\alpha\beta3}$	W	S	W	
$^3J_{N\beta2}$	S	W	W	HNHB
$^3J_{N\beta3}$	W	W	S	
$^3J_{C\beta2}$	W	S	W	HN(CO)HB
$^3J_{C\beta3}$	S	W	W	
ROEs				
$\alpha-\beta_2$	S	S	W	^{13}C ROESY
$\alpha-\beta_3$	S	W	S	
NH-β_2	W	S	S	^{15}N ROESY
NH-β_3	S	S	W	

FIGURE 1: Scheme for obtaining stereospecific assignments of β-methylene protons and χ_1 rotamers on the basis of a qualitative analysis of the relative intensities of cross peaks observed in the 3D ^{15}N-edited ROESY, ^{13}C-edited ROESY, ^{15}N-edited HOHAHA, HNHB, and HN(CO)HB experiments (Clore et al., 1991a; Archer et al., 1991; Grzesiek et al., 1992). The relative intensities of the NH-C^βH cross peaks in the 3D ^{15}N-edited HOHAHA, HNHB, and HN(CO)HB spectra are dependent on the size of the $^3J_{\alpha\beta}$, $^3J_{NH\beta}$, and $^3J_{COH\beta}$ coupling constants, respectively, where a large coupling constant (i.e., trans conformation) results in a strong cross peak. The expected pattern of cross-peak intensities is indicated for the three preferred χ_1 rotamers ($-60°$, $180°$, and $+60°$). A strong cross peak is indicated by the letter S, and a weak or missing peak is indicated by the letter W. Analysis of high-resolution well-refined X-ray structures indicates that <20% of χ_1 angles deviate by more than 20° from the staggered rotamer positions (Ponder & Richards 1987; McGregor et al., 1987; Nilges et al., 1990).

The majority of the β-methylene stereospecific assignments and the ϕ, ψ, and χ_1 torsion angle restraints were obtained from $^3J_{NH\alpha}$ coupling constants, and approximate distance restraints for intraresidue and sequential NOEs involving NH, $C^\alpha H$, and $C^\beta H$ protons were obtained by means of the conformational grid search program STEREOSEARCH (Nilges et al., 1990), as described previously (Kraulis et al., 1989). These were verified and in some cases extended on the basis of the relative intensities of cross peaks observed in the 3D ^{15}N- and ^{13}C-edited ROESY, ^{15}N-edited HOHAHA, HNHB, and HN(CO)HB experiments, as depicted in Figure 1. Stereospecific assignments for the methyl groups of the valine residues were obtained on the basis of the relative intensity of the intraresidue NH–C^γH and C^αH–C^γH NOEs as described by Zuiderweg et al. (1985).

The Ile and Leu χ_2 torsion angle restraints, as well as the stereospecific assignment of the methyl groups of the Leu residues, were determined from $^3J_{C\alpha C\delta}$ coupling constants obtained from the relative intensity of the C^α and C^δ cross peaks in a 3D long-range ^{13}C–^{13}C NMR correlation spectrum (Bax et al., 1992), in conjunction with the relative intensities of intraresidue NOEs involving NH, $C^\alpha H$, $C^\gamma H$, and $C^\delta H$ protons expected for the three χ_1 rotamers (Table I). The latter are necessary to distinguish χ_2 angles of 60° and 180° for Leu and –60° and +60° for Ile. These restraints were verified by examining the resulting structures for consistency with the long-range NOEs involving the methyl groups of Ile and Leu. An example of a typical $^1H(F_3)-^{13}C(F_1)$ plane of the 3D long-range ^{13}C–^{13}C correlation spectrum is illustrated in Figure 2.

Cysteine disulfide bridge χ_2 and χ_3 torsion angle restraints were based on the following: (a) a comparison of the C^α–$C^{\alpha'}$

Table I: $^3J_{C\alpha C\delta}$ Coupling Constants and the Pattern of Intraresidue NOEs Employed for Determining the Stereospecific Assignments of Methyl Groups of Leu and χ_2 Torsion Angle Restraints for Leu and Ile[a]

χ_2	Leu			Ile		
	180°	–60°	60°	180°	–60°	60°
	Long-Range C–C Couplings					
$^3J_{C\alpha C\delta 1}$ (Hz)	≥3	<1.2	<1.2	≥3	<1.2	<1.2
$^3J_{C\alpha C\delta 2}$ (Hz)	<1.2	<1.2	≥3			
	Intraresidue NOEs					
$\chi_1 = 180°$						
$C^\alpha H$–$C^\gamma H$	s	w	m			
$C\alpha H$–$C^{\delta 1}H$	w	w	s	s	w	m
$C^\alpha H$–$C^{\delta 2}H$	m	s	w			
NH–$C^\gamma H$	w	w	w			
NH–$C^{\delta 1}H$	w	w	w	w	m	m
NH–$C^{\delta 2}H$	w	w	w			
$C^{\gamma m}H$–$C^{\delta 1}H$				m	w	m
$\chi_1 = -60°$						
$C^\alpha H$–$C^\gamma H$	m	w	s			
$C\alpha H$–$C^{\delta 1}H$	w	s	m	m	w	s
$C^\alpha H$–$C^{\delta 2}H$	s	m	w			
NH–$C^\gamma H$	s	w	w			
NH–$C^{\delta 1}H$	w	w	s	w	m	m
NH–$C^{\delta 2}H$	w	w	s			
$C^{\gamma m}H$–$C^{\delta 1}H$				m	w	m
$\chi_1 = 60°$						
$C^\alpha H$–$C^\gamma H$	w	w	w			
$C\alpha H$–$C^{\delta 1}H$	w	w	w	w	w	w
$C^\alpha H$–$C^{\delta 2}H$	w	w	w			
NH–$C^\gamma H$	m	w	s			
NH–$C^{\delta 1}H$	w	s	m	w	m	m
NH–$C^{\delta 2}H$	w	m	w			
$C^{\gamma m}H$–$C^{\delta 1}H$				m	w	m

[a] The pattern NOEs, classified as strong (s), medium (m), and weak (w), for the various pairs of χ_1 and χ_2 torsion angles was obtained by examining the corresponding interproton distances using the molecular graphics program FRODO (Jones, 1978).

distances observed in the simulated annealing (SA) structures calculated during the course of the iterative refinement, with a crystal data base relating the C^α–$C^{\alpha'}$ distance to the χ_1, χ_2, and χ_3 torsion angles (Richardson, 1981), and (b) on an analysis of the clustering of the χ_2 and χ_3 angles observed in the NMR structures obtained at a late stage of the refinement procedure. Since the N- and C-termini are disordered, the distribution of C^α–$C^{\alpha'}$ distances between Cys 7 an Cys 131 was large, so that no χ restraints could be obtained for this disulfide bridge. The minimum ranges employed for the ϕ, ψ, and χ torsion angle restraints were ±30°, ±50°, and ±20°, respectively (Kraulis et al., 1989).

Hydrogen-Bonding Restraints. The hydrogen bond restraints were deduced on the basis of slowly exchanging NH protons and the pattern of sequential and interstrand NOEs involving the NH and $C^\alpha H$ protons (Wüthrich, 1986). Slowly exchanging NH protons were identified from a series of 2D ^{15}N–^1H Overbodenhausen correlation spectra (Bodenhausen & Ruben, 1980; Bax et al., 1990; Norwood et al., 1990) acquired over a period of ~24 h starting within 5 min of dissolving an unexchanged sample of lyophilized protein in D_2O [see Garrett et al. (1992)]. Two distance restraints were used for each hydrogen bond: one between the hydrogen and the acceptor atom of 1.5–2.3 Å and one between the donor heavy atom and the acceptor atom of 2.4–3.3 Å. These were only introduced subsequent to the initial set of structure calculations.

Structure Calculations. Structures were calculated using the hybrid distance geometry–dynamical simulated annealing method of Nilges et al. (1988a) with minor modifications (Clore et al., 1990b), making use of the program XPLOR
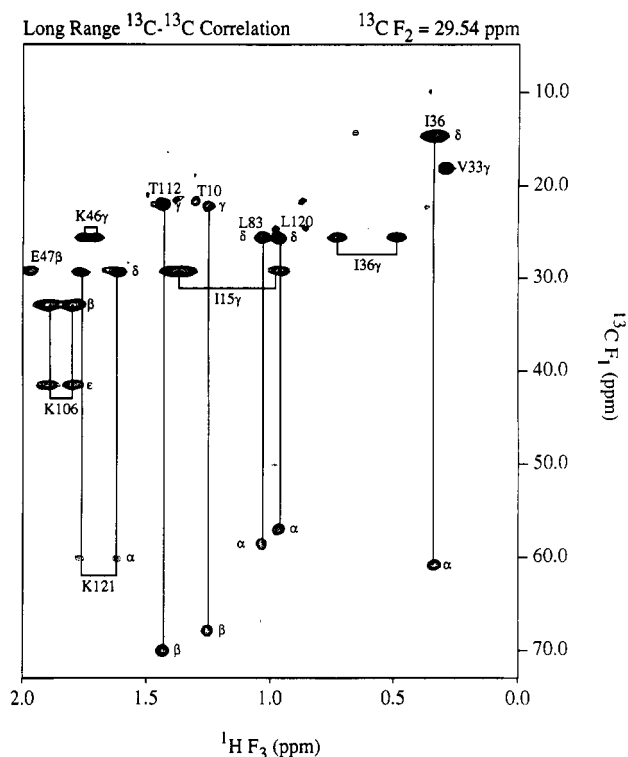

Long Range ^{13}C-^{13}C Correlation ^{13}C F_2 = 29.54 ppm

FIGURE 2: Example of a $^{13}C(F_1)$–$H(F_3)$ plane taken at $^{13}C(F_2)$ = 29.54 ppm of the 3D ^{13}C–^{13}C long-range correlation spectrum of IL-4. Because of the large disparity in the intensity of cross peaks in the C^α region (equivalent to cross peaks arising from long-range ^{13}C–^{13}C three-bond couplings) and the C^γ/C^δ region (equivalent to diagonal peaks), these two regions are plotted at different threshold levels and superimposed onto one plot for clarity. (The starting contour level is a factor of 2 lower for the diagonal peaks.) The relative intensities of the C^α and C^δ cross peaks for Ile 36, Leu 83, and Leu 120 were used directly to determine the $^3J_{C\alpha C\delta}$ coupling constants ($^3J_{C\alpha C\delta} = \tan^{-1}\{|I_{cross}/I_{diag}|^{1/2}\}/2\pi\tau$, where I_{cross} and I_{diag} are the intensities of the $C^\alpha(F_1)$–$C^\delta H(F_3)$ and $C^\delta(F_1)$–$C^\delta H(F_3)$ cross peaks, respectively, and $2\tau = 1/^1J_{CC} = 29.4$ ms), from which information on the corresponding χ_2 torsion angles was derived. Negative cross peaks are indicated by dashed contour lines.

(Brünger et al., 1986; Brünger, 1992; Kuszewski et al., 1992). The protocol involves calculating an initial set of substructures incorporating only one-third of the atoms by projection from n-dimensional distance space into Cartesian coordinate space, followed by simulated annealing with all atoms. The target function that is minimized during simulated annealing (as well as during conventional Powell minimization) comprises *only* quadratic harmonic terms for covalent geometry (that is, bonds, angles, planes, and chirality), square-well quadratic potentials for the experimental distance and torsion angle restraints (Clore et al., 1986), and a quartic van der Waals repulsion term for the nonbonded contacts (Nilges et al., 1988a–c). All peptide bonds were constrained to be planar and trans. There were *no* hydrogen-bonding, electrostatic, or 6–12 Lennard-Jones empirical potential energy terms in the target function.

Iterative Structure Refinement. As in previous structure determinations form this laboratory (Kraulis et al., 1989; Clore et al., 1990b, 1991c; Omichinski et al., 1990; Forman-Kay et al., 1991; Gronenborn et al., 1991), an iterative refinement strategy was employed, incorporating more experimental restraints at each successive stage as the quality of the structure improves. The starting point for the current refinement was the initial second generation structure of IL-4 (Powers et al., 1992b). This structure was based on a total of 921 NOE restraints without stereospecific assignments and 183 backbone (ϕ, ψ) torsion angle restraints, and it had a backbone atomic

rms distribution about the mean coordinate positions of 0.95 ± 0.16 Å for residues 8–129.

Using an iterative approach, we were able to resolve all ambiguities in the assignment of NOEs from the 3D ^{15}N- and ^{13}C-edited and 4D ^{15}N/^{13}C- and ^{13}C/^{13}C-edited NOESY experiments. Thus, it was required that the assignment of any given ambiguous NOE must be consistent with the current structure, thereby eliminating unreasonable assignments with interproton distances greater than 6 Å. More importantly, the current refined structure also aided in the identification of misassigned NOEs, which arose as a result of the very limited ^{1}H chemical shift dispersion exhibited by the IL-4 spectrum (Powers et al., 1992a). The simulated annealing calculation was then repeated after each update of the restraint list, and a new set of structures was generated for further analysis of the NMR data.

Since the 3D and 4D heteronuclear-edited NOESY spectra were recorded with mixing times ranging from 100 to 150 ms, it was apparent that the classification of NOEs into strong, medium, and weak categories could be influenced by spin-diffusion effects. Consequently, NOEs in the restraint list were evaluated for spin-diffusion effects at each iteration on the basis of observed distances and spatial relationships in the current ensemble of structures. If the resulting distance was significantly longer than that predicted from an isolated two-spin interpretation of the experimentally observed NOE intensity, and a spin-diffusion pathway was highly probable on the basis of the spatial geometry of the relevant protons, as well as a qualitative interpretation of NOE intensities calculated by a full-relaxation matrix procedure (Brünger, 1992), the corresponding upper bound distance limit for the NOE was either adjusted upward (i.e., into the next distance range class if the NOE was originally classified as strong or medium) or the NOE was removed from the restraint list (if the NOE was originally classified as weak). This procedure was employed specifically for two types of situations: first, in cases where two methylene protons (attached to the same carbon) exhibit an NOE to the same spin, but one of the two methylene protons clearly points away from this spin at a distance greater than 5 Å; second, in cases where the complete ring system of a Phe shows NOEs to a particular spin, but where it is clear from the spatial configuration that only the C$^\zeta$H proton is actually close in space to this spin (i.e., so that the NOEs observed to the C$^\delta$H and C$^\epsilon$H protons arise from an indirect cross-relaxation pathway via the C$^\zeta$H proton).

As the approximate interproton distance restraints are classified into three ranges, the resulting distinct cutoffs can result in systematic errors for interproton distances whose values lie at the boundary of two distance ranges. This can be corrected by examining the distribution of violations in the ensemble of calculated structures (Clore et al., 1993). Thus, if a particular interproton distance restraint was systematically violated in all of the structures, even by as little as 0.1 Å, we reclassified it into the next class (i.e., from strong to medium and from medium to weak), as discussed by Clore et al. (1993).

From our experience, a conservative approach to the assignment of NOE restraints results in more accurate structures, even if this is achieved at the expense of a slight decrease in precision. Thus, as the lower bound is always set to the sum of the van der Waals radii of two protons (i.e., 1.8 Å), an increase in the upper bound limit of an NOE restraint simply reduces its information content but does not introduce any errors. Conversely, an erroneous NOE or an NOE that is incorrectly assigned to a stronger class (i.e., a smaller upper bound) will introduce errors in the restraint list and conse-

quently have a detrimental effect on the accuracy of the structure. A typical example would be the observation of a skewed χ_1 rotamer conformation in a case where the coupling constants clearly indicate that the χ_1 angle lies in one of the three preferred conformations (i.e., 60°, –60°, or 180°); another example would be the observation of a single, tightly clustered, skewed χ_1 rotamer conformation in a case where the coupling constants are clearly indicative of multiple rotamer populations.

The large number of fully processed 2D planes in the 4D ^{15}N/^{13}C- and ^{13}C/^{13}C-edited NOESY spectra (4096 and 16 384, respectively) required novel processing tools for analysis. The new tools incorporate the current set of refined structures, the XPLOR interproton distance restraint list, and the chemical shift (^{1}H, ^{15}N, and ^{13}C) assignment table with the 4D data into the programs PIPP and STAPP (Garrett et al., 1991; D. S. Garrett, unpublished) to identify potentially unassigned cross peaks in the 4D NMR spectra. The program STAPP identifies potential new interproton distance restraints from the 4D NOE spectra that are consistent with the chemical shift assignments, have interproton distances of less than 6 Å in the current set of structures, and are not in the XPLOR interproton distance restraint list. The cross peaks associated with the new interproton distance restraints can then be examined visually using PIPP to verify the presence of a real peak or to eliminate artifacts. This approach greatly facilitated the analysis of the 4D NOE spectra and permitted the incorporation of a substantial number of new NOEs into the restraint list. Indeed, the 4D ^{13}C/^{13}C-edited NOESY spectrum was particularly valuable in the identification of NOEs between methyl protons with very similar or identical ^{1}H chemical shifts.

Examples of the quality of the 4D ^{13}C/^{13}C-edited NOESY and 4D ^{15}N/^{13}C-edited NOESY spectra are provided in Figures 3 and 4, respectively. Figure 3 shows two 2D cross-sections taken through the 4D ^{13}C/^{13}C-edited NOESY spectrum, perpendicular to the F_3(^{13}C) and F_4(^{1}H) coordinates of the C$^\delta$ methyl group of Ile 36 and the C$^\epsilon$ methylene group of Lys 88. Figure 4 shows a 2D cross-section taken through the 4D ^{15}N/^{13}C-edited NOESY spectrum, perpendicular to the F_2(^{15}N) and F_4(^{1}H) coordinates for the NH groups of Ile 9, Phe 77, Val 105, Glu 107, and Phe 116.

At the end of the iterative refinement cycle, stereospecific assignments were obtained for 52 of the 96 residues with β-methylene protons, for the methyl groups of two of the three Val residues, and for the methyl groups of 13 of the 16 Leu residues. The majority of the residues without stereospecific assignments corresponded to surface residues with disordered side chains or residues with degenerate β-methylene protons. The validity of the stereospecific assignments was confirmed by being properly accounted for in further refined structures. A table of the complete ^{1}H, ^{13}C, and ^{15}N assignments of IL-4, including all stereospecific assignments obtained, is provided in the supplementary material.

For well-defined Phe and Tyr residues, the NOE distance restraints to the C$^\delta$H and C$^\epsilon$H protons can often be assigned to only one side of the ring, thereby discriminating between the C$^{\delta 1}$H and C$^{\delta 2}$H or the C$^{\epsilon 1}$H and C$^{\epsilon 2}$H protons (Forman-Kay et al., 1991a). In the case of IL-4, all six Phe and both Tyr residues were well defined and had low surface accessibilities, making it possible to assign NOE restraints to only one of the pair of C$^\delta$H and C$^\epsilon$H protons when it was clear that the NOE could only be to one of them.

$^1J_{C\alpha H\alpha}$ coupling constants obtained from a coupled 3D CT-HCACO spectrum were used to ascertain the presence of
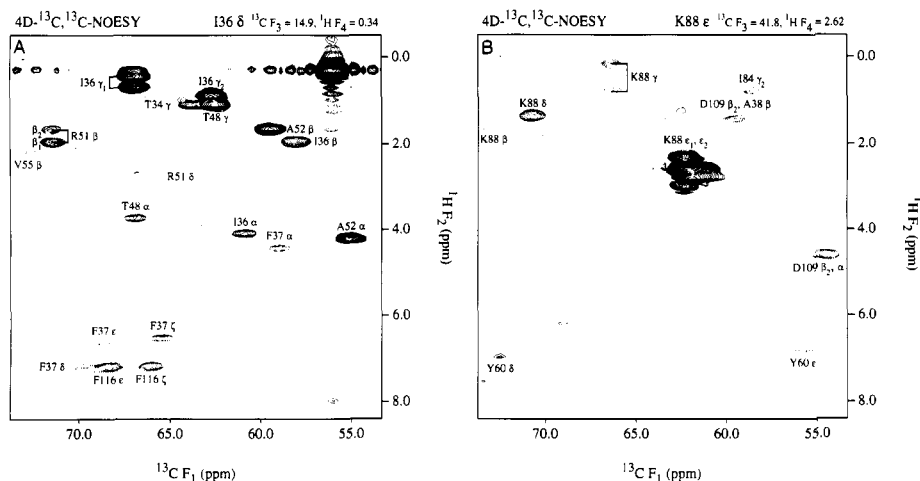
FIGURE 3: Examples of typical $^{13}C(F_1)-^1H(F_2)$ planes taken at two different $^{13}C(F_3)-^1H(F_4)$ cross-sections through the 4D $^{13}C/^{13}C$-edited NOESY spectrum of IL-4. The cross-sections shown correspond to the ^1H and ^{13}C chemical shifts of (A) Ile 36 δ and (B) Lys 88 ϵ, with partial overlap of Asp 109 β_2. These cross-sections display $^1H-^{13}C$ correlations of protons that have an NOE interaction with (A) Ile $C^\delta H$ and (B) Lys 88 $C^\epsilon H$ or Asp 109 $C^{\beta 2}H$. Since the spectral width in the ^{13}C dimension was set to 20.71 ppm, resonances were extensively folded in F_1 and F_3 resulting in both negative and positive cross peaks. Negative cross peaks are indicated by dashed contour lines.
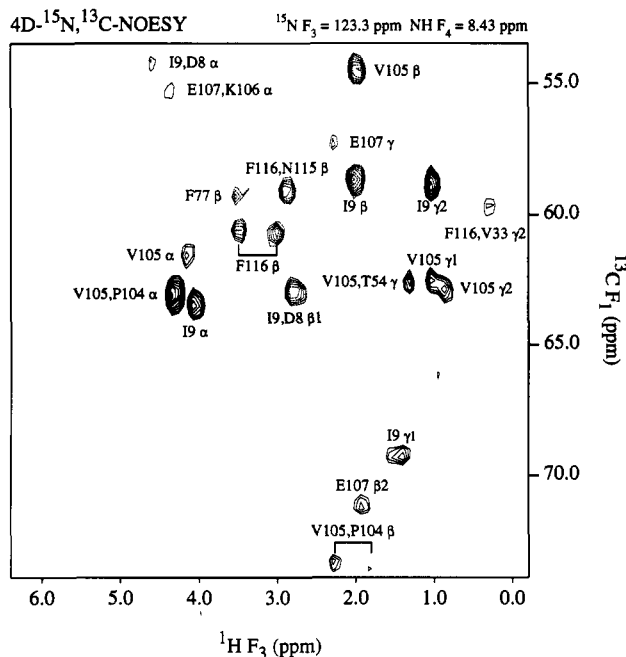
FIGURE 4: Example of a typical $^{13}C(F_1)-^1H(F_3)$ plane taken at the $^{15}N(F_2) = 123.3$ ppm and NH(F_4) = 8.43 ppm cross-section through the 4D $^{15}N/^{13}C$-separated NOESY spectrum of IL-4. The cross-section shown corresponds to the ^{15}N and NH chemical shifts of residues Ile 9, Phe 77, Val 105, Glu 107, and Phe 116 and displays $^1H-^{13}C$ correlations of protons that have an NOE interaction with the backbone amide protons of these residues. Since the spectral width in the ^{13}C dimension was set to 20.71 ppm, resonances were extensively folded in F_1 resulting in both negative and positive cross peaks. Negative cross peaks are indicated by dashed contour lines.

non-glycine residues with positive ϕ backbone torsion angles, since a value of less than 134 Hz is indicative of a positive ϕ torsion angle (Vuister et al., 1992). No values less than 134 Hz were observed. Hence, all non-glyine ϕ torsion angles were, as a minimum, restrained to be negative ($-2°$ to $-178°$), provided that the corresponding $^1J_{C\alpha H\alpha}$ coupling constant could be accurately measured from the 3D CT-HCACO spectrum. In addition, some ϕ and ψ torsion angle restraints were added for defined backbone regions where the ϕ and ψ torsion angles in the current set of structures had observed ranges of less than $\pm 20°$. The boundaries for these restraints, however, were significantly larger ($\pm 50°$) than the observed $\pm 20°$ range.

Hence, the purpose of incorporating these restraints was not to increase the precision of the local structure but to assist in the convergence of the simulated annealing calculations.

The incorporation of ψ restraints in the simulated annealing protocol can be problematic in regions which do not correspond to secondary structure elements. Therefore, most ψ restraints were added near the end of the iterative refinement procedure when the structures were fairly well defined and most, if not all, erroneous interproton distance restraints were corrected. It was our empirical observation that the quality and precision of each ensemble of structures were primarily dependent on the number and correctness of the interproton distance restraints employed in the simulated annealing calculations. The presence of torsion restraints mainly assists in the convergence rate of the calculations, particularly since the torsion angle restraint boundaries were always much larger than the resulting standard deviations for the corresponding torsion angles in the calculated ensemble of structures.

The final 30 simulated annealing structures were calculated on the basis of 2973 experimental NMR restraints. These comprised 2515 approximate interproton distance restraints which were subdivided as follows: 522 interresidue sequential ($|i - j| = 1$), 549 interresidue short-range ($1 < |i - j| \le 5$), 560 interresidue long-range ($|i - j| > 5$), and 884 intraresidue restraints; 102 distance restraints for 51 backbone hydrogen bonds; and 356 torsion angle restraints subdivided into 130 ϕ, 119 ψ, 73 χ_1, 32 χ_2, and 2 χ_3 torsion angle restraints. The complete set of coordinates and experimental restraints has been deposited in the Brookhaven Protein Data Bank.

Tightly Bound Water. Upon completion of the simulated annealing calculations, we identified the presence of two tightly bound water molecules (lifetime > 1 ns) in the IL-4 structure from the 3D ^{15}N-edited ROESY spectrum by the observation of ROEs from the water frequency to NH protons (Otting & Wüthrich, 1989; Clore et al., 1990a; Forman-Kay et al., 1991b; Clore & Gronenborn, 1992). The 3D ^{15}N-edited ROESY experiment for the $F_1(^1H)$ plane corresponding to the chemical shift of water (4.67 ppm) is illustrated in Figure 5. The cross peaks corresponding to ROEs between bound water (W) and the side-chain NH_2 groups of Gln 24, Gln 76, and Gln 82 are indicated. The two bound water molecules were *not* included in the refinement process because of the difficulty of correctly placing the water molecules in the structure. A number of other cross peaks to bound water are also observed in this
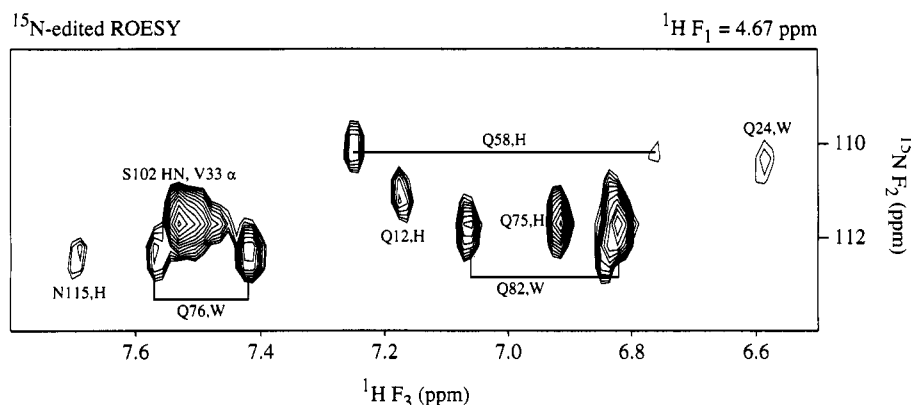
FIGURE 5: Expanded $^{15}N(F_2)$–$^1H(F_3)$ plane corresponds to the NH_2 region taken at the $^1H(F_1)$ frequency of water (4.67 ppm) of the 3D ^{15}N-edited ROESY spectrum of IL-4. The ROE cross peaks to bound water are indicated by the letter W. ROE cross peaks whose origins could not be distinguished between direct ROEs with bound water or ROEs coupled to chemical exchange with water through a neighboring side-chain-exchangeable group (e.g., $N^\zeta H^{3+}$ of Lys, guanidinium group of Arg, and OH group of Ser, Thr, and Tyr) are indicated by the letter H.

spectrum, but they potentially arise from an indirect process involving chemical exchange between water and a rapidly exchanging group (e.g., the hydroxyl group of Ser or Thr).

RESULTS AND DISCUSSION

The Converged Structures. The structural statistics for the final 30 simulated annealing (SA) structures of human IL-4 are summarized in Table II, and best fit superpositions of the backbone atoms and selected side chains are shown in Figures 6 and 7, respectively. The atomic rms distributions about the mean coordinate positions and the angular rms deviations for the ϕ, ψ, χ_1, and χ_2 torsion angles, together with the variations in surface accessibility, are shown in Figure 8 as a function of residue number. As is evident from the data in Figures 6–8, the final structures are of high precision and accuracy. In addition, they display very small deviations from idealized covalent geometry and satisfy the experimental NMR restraints within experimental errors (Table II). Thus, there are no interproton distance and torsion angle violations greater than 0.1 Å and 1°, respectively. There are no bad nonbonded contacts, as indicated by the small value of the quartic van der Waals repulsion term, F_{repel} (3.4 kcal mol^{-1}). This is further supported by the calculated value of two other energy parameters which were *not* included in the target function for simulated annealing, namely, the large negative values for the Lennard-Jones–van der Waals energy (–466 ± 10 kcal mol^{-1}) and the solvation free energy of unfolding (–133 ± 3 kcal mol^{-1}). The latter is consistent with a protein the size of IL-4 (Eisenberg & McLachlan, 1986; Chiche et al., 1990) and is indicative of an appropriate distribution of hydrophobic and hydrophilic residues within the interior and exterior of the protein.

Excluding residues 1–7 and 130–133 at the N- and C-termini, which are poorly defined by the data (cf. Figure 8), the atomic rms distribution of the 30 SA structures about the mean coordinate positions is 0.44 ± 0.33 Å for the backbone atoms, 0.83 ± 0.03 Å for all atoms, and 0.51 ± 0.04 Å for all atoms excluding disordered surface side chains (Table II). In addition, the mean standard deviations for the ϕ and ψ backbone torsion angles of residues 8–129 are 8.4 ± 7.0° and 8.4 ± 6.8°, respectively. The backbone of the core of the protein comprising the elements of regular secondary structure is defined to an even greater degree of precision and accuracy, with an atomic rms distribution about the mean coordinate positions of 0.34 ± 0.04 Å and mean standard deviations of 6.1 ± 4.2° and 6.3 ± 3.9° for the ϕ and ψ backbone torsion

angles, respectively. Not surprisingly, surface side chains, and in particular residues with longer side chains such as Lys and Arg, tend to be partially disordered, especially beyond the C^γ position. This is clearly evident in Figure 8, where the standard deviations of the χ_1 and χ_2 torsion angles are plotted together with surface accessibility as a function of residue. In addition to the N- and C-termini, the largest backbone atomic and angular (ϕ,ψ) rms deviations occur in the surface-exposed loop regions comprising residues 25–31, 35–43, 67–72, and 99–109 (Figures 6 and 8), which correlates with their higher degree of mobility as seen in ^{15}N relaxation measurements (Redfield et al., 1992).

Most of the backbone torsion angles for non-glycine residues lie within the allowed and expected α-helix and β-sheet regions of the Ramachandran plot (Figure 9). The few non-glycine residues that fall outside these regions correspond to residues located at the structural interfaces of helices and connecting loops (Ala 72, Asp 109), in loop regions (Ile 36, Lys 41, and Lys 106), or at the C-terminus (Lys 130). Gly 99 and Gly 71 are the only residues which exhibit a positive ϕ angle.

The backbone atomic rms shift from the average coordinates of our previous second generation structure (Powers et al., 1992b) to the average coordinates of the present high-resolution fourth generation structure is $\sim$1.7 Å (for residues 8–129). This difference is $\sim$0.3 Å larger than the sum of the backbone atomic rms deviations of the two ensembles of simulated annealing structures about their respective means. Hence, the previous average coordinates lie just outside the current ensemble of highly refined simulated annealing structures. This finding is completely in line with previous observations on the determination of the solution structure of interleukin-1β at various stages of refinement (Clore et al., 1990c, 1991c), as well as with a series of extensive theoretical calculations aimed at probing the effects of the number of experimental NMR restraints on the precision and accuracy of the resulting coordinates (Clore et al., 1993). In particular, an increase in the number of restraints not only reduces the atomic rms spread of the ensemble of simulated annealing structures but also results in a concomitant and significant increase in the accuracy of both the ensemble and mean coordinates. Further, the precision of an ensemble of structures is always greater than its accuracy (Clore et al., 1993). Indeed, in model calculations the backbone rms difference between an ensemble of NMR structures and the true structure (i.e., the accuracy) is 50–70% larger than the corresponding rms difference between the same ensemble of structures and their mean coordinate

Table II: Structural Statistics and Atomic rms Differences[a]

A. Structural Statistics

	$\langle SA \rangle$	$\overline{(SA)}r$	X-ray[b]
rms deviations from exptl distance restraints (Å)[c]			
all (2617)	0.0016 ± 0.0009	0.0043	0.609
interresidue sequential ($|i - j| = 1$) (522)	0.0022 ± 0.0019	0.0061	0.457
interresidue short-range ($1 < |i - j| \leq 5$) (549)	0.0013 ± 0.0015	0.0044	0.941
interresidue long-range ($|i - j|) > 5$) (560)	0.0009 ± 0.0003	0.0021	0.792
intraresidue (884)	0.0009 ± 0.0007	0.0038	0.163
H-bonds (102)[d]	0.0027 ● 0.0008	0.0053	0.084
rms deviations from exptl dihedral restraints (deg) (356)[c,e]	0.068 ± 0.020	0.121	32.9
F_{NOE} (kcal mol^{-1})[f]	0.45 ± 0.69	2.40	48234
F_{tor} (kcal mol^{-1})[f]	0.11 ± 0.07	0.315	23108
F_{repel} (kcal mol^{-1})[f]	3.39 ± 0.82	20.77	1081
F_{L-J} (kcal mol^{-1})[g]	−466 ± 10	−477	−368
E_{SFE} (kcal mol^{-1})[h]	−133 ± 3	−149	−141
deviations from idealized covalent geometry			
bonds (Å) (2175)	0.001 ± 0	0.002	0.028
angles (deg) (3929)	0.209 ± 0.006	0.279	5.593
impropers (deg) (835)[i]	0.175 ± 0.026	0.206	3.239

B. Atomic rms Differences (Å)

	residues 8–129		secondary structure[j]		ordered side chains[k]
	backbone atoms	all atoms	backbone atoms	all atoms	all atoms
$\langle SA \rangle$ vs $\overline{SA}$	0.44 ± 0.03	0.83 ± 0.03	0.34 ± 0.04	0.78 ± 0.04	0.51 ± 0.04
$\langle SA \rangle$ vs $\overline{(SA)}r$	0.46 ± 0.03	0.91 ± 0.04	0.36 ± 0.04	0.86 ± 0.05	0.54 ± 0.04
$\overline{(SA)}r$ vs $\overline{SA}$	0.13	0.37	0.11	0.37	0.18
$\overline{SA}$ vs X-ray	1.35	2.16	1.04	1.88	1.73
$\overline{(SA)}r$ vs X-ray	1.37	2.24	1.04	1.94	1.76
$\langle SA \rangle$ vs X-ray	1.42 ± 0.04	2.31 ± 0.05	1.09 ± 0.07	2.03 ± 0.06	1.81 ± 0.04

[a] The notation of the NMR structures is as follows: $\langle SA \rangle$ are the final 30 simulated annealing structures; $\overline{SA}$ is the mean structure obtained by averaging the coordinates of the individual SA structures best fit to each other (excluding residues 1–7 and 130–133); and $\overline{(SA)}r$ is the restrained minimized mean structure obtained by restrained regularization of the mean structure $\overline{SA}$ (Nilges et al., 1988a). The number of terms for the various restraints is given in parentheses. [b] X-ray is the 2.25 Å resolution X-ray structure of Wlodawer et al. (1988). [c] None of the structures exhibited distance violations greater than 0.1 Å or dihedral angle violations greater 1°. [d] For each backbone NH–CO hydrogen bond there are two restraints: r_{NH-O} = 1.5–2.3 Å and r_{N-O} = 2.5–3.3 Å. All hydrogen bonds involve slowly exchanging NH protons. [e] The torsion angle restraints comprise 130 ϕ, 119 ψ, 73 χ_1, 32 χ_2, and 2 χ_3 restraints. [f] The values of the square-well NOE (F_{NOE}) and torsion angle (F_{tor}) potentials [cf. eqs 2 and 3 in Clore et al. (1986)] are calculated with force constants of 50 kcal mol^{-1} Å^{-2} and 200 kcal mol^{-1} rad^{-2}, respectively. The value of the quartic van der Waals repulsion term F_{rep} [cf. eq 5 in Nilges et al. (1988a)] is calculated with a force constant of 4 kcal mol^{-1} Å^{-4} with the hard-sphere van der Waals radius set to 0.8 times the standard values used in the CHARMM (Brooks et al., 1983) empirical energy function (Nilges et al., 1998a–c). [g] E_{L-J} is the Lennard-Jones–van der Waals energy calculated with the CHARMM (Brooks et al., 1983) empirical energy function and is *not* included in the target function for simulated annealing or restrained minimization. [h] E_{SFE} is the calculated solvation free energy of folding (Eisenberg & McLachlan, 1986; Chiche et al. 1990) and is *not* included in the target function of simulated annealing or minimization. The expected value of E_{SFE} for a protein the size of human recombinant IL-4 (133 residues) is −135 kcal mol^{-1} (Chiche et al., 1990). [i] The improper torsion restraints serve to maintain planarity and chirality. [j] The residues in regular secondary structure are residues 8–24 (α_A), 32–34 (β_A), 44–66 (α_B), 73–98 (α_C), and 110–128 (β_B and α_D). [k] The disordered side chains that were excluded are as follows: residues 1–8; residues 131–133; Gln 12 beyond the C$^\delta$ position; Glu 13 from the C$^\delta$ position onward; Lys 16 from C$^\delta$; Glu 23 from C$^\delta$; Gln 16 from C$^\delta$; Lys 25 from C$^\epsilon$; Leu 27 beyond C$^\gamma$; Glu 30 from C$^\delta$; Lys 41 from C$^\gamma$; Asp 42 from C$^\gamma$; Thr 44 beyond C$^\beta$; Glu 45 from C$^\delta$; Lys 46 from C$^\epsilon$; Glu 47 from C$^\delta$; Arg 51 from N$^\epsilon$; Arg 57 from C$^\delta$; Gln 58 beyond C$^\delta$; His 62 beyond C$^\gamma$; Glu 64 from C$^\delta$; Lys 65 from C$^\epsilon$; Asp 66 beyond C$^\gamma$; Thr 67 beyond C$^\beta$; Arg 68 from C$^\delta$; Thr 73 beyond C$^\beta$; Gln 75 from C$^\delta$; Gln 76 from C$^\delta$; Arg 79 from C$^\delta$; Lys 81 from C$^\delta$; Gln 82 from C$^\gamma$; Arg 85 from C$^\gamma$; Lys 88 from C$^\delta$; Arg 89 from N$^\epsilon$; Asp 91 beyond C$^\gamma$; Arg 92 from C$^\delta$; Asn 93 from C$^\gamma$; Leu 100 beyond C$^\gamma$; Asn 101 from C$^\gamma$; Ser 102 beyond C$^\beta$; Lys 106 from C$^\gamma$; Glu 107 beyond C$^\gamma$; Asp 109 beyond C$^\gamma$; Gln 110 from C$^\delta$; Glu 114 from C$^\delta$; Asn 115 beyond C$^\gamma$; Glu 118 from C$^\delta$; Arg 119 from N$^\epsilon$; Lys 121 from C$^\epsilon$; Arg 125 from C$^\beta$; Glu 126 from C$^\delta$; Lys 127 from C$^\delta$; Ser 129 beyond C$^\beta$; and Lys 130 from Cδ.

positions (i.e., the precision), independent of the number of experimental NMR restraints, provided these are sufficient to define the polypeptide fold (Clore et al., 1993).

There are a number of reasons for the above observations. First, as the nonbonded contacts are represented by a simple quartic van der Waals repulsion term, the only attractive forces present in the target function are those associated with the interproton distance restraints. Hence, the lower the number of interproton distance restraints, the smaller the contribution of the attractive forces to the target function, which will tend to result in a systematic expansion of the calculated structures (Clore et al., 1993). Second, the exact backbone conformation is critically dependent on the detailed packing of internal side chains, which in the case of IL-4 involves an unusually large number of Leu and Ile residues. If the side-chain conformations of these internal Leu and Ile residues, as well as those of the other hydrophobic residues within the protein core, are poorly defined due to either a small number of interproton

distance restraints or the absence of stereospecific assignments and associated χ_1 and χ_2 torsion angle restraints, the correct packing of their side chains will not be attained. As a result, the probability of generating, under these circumstances, either an individual structure or an average structure which is very close to the true structure is likely to be infinitesimally small (Clore et al., 1990c). In this respect, it should be noted that the experimental restraints used to compute the earlier low-resolution structures did *not* include any stereospecific assignments or side-chain torsion angle restraints (Powers et al., 1992b; Smith et al., 1992). In addition to these two factors, which are intrinsic to NMR protein structure determination, it should be kept in mind that the experimental NMR restraints used to calculate the low-resolution structures are likely to contain errors (e.g., misassignment of NOEs, incorrect torsion angle restraints). That this is clearly the case can be ascertained by examining the overall rms of the violations of all upper interproton distance bounds, and all upper and lower
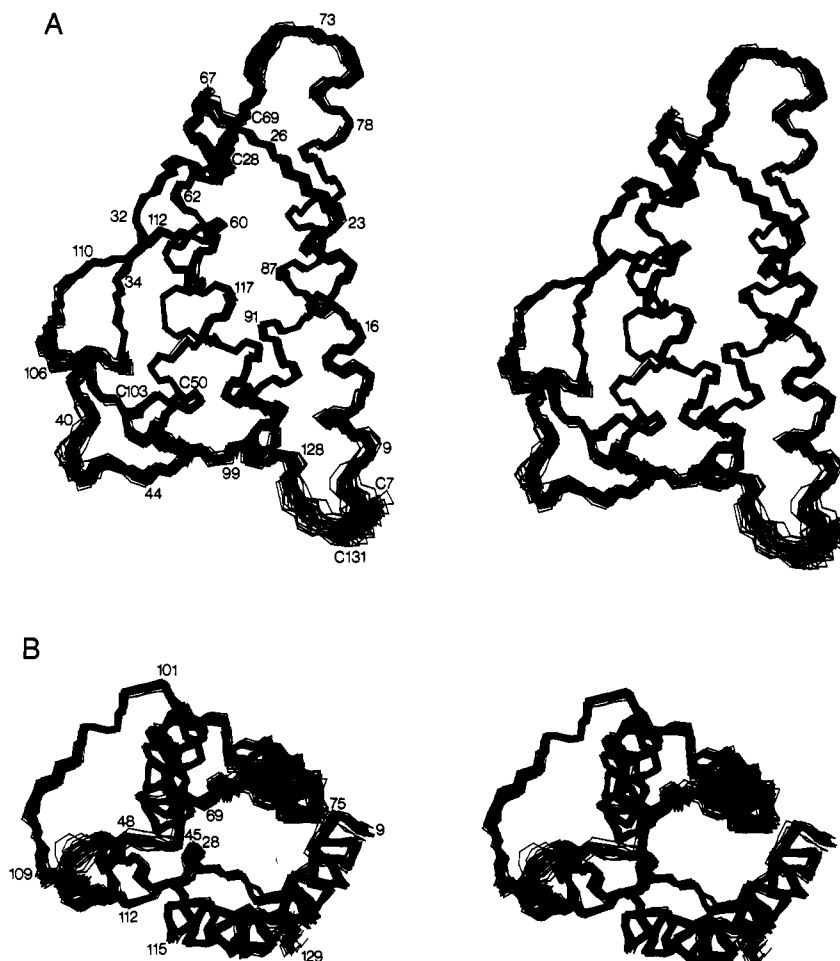
FIGURE 6: Two stereoviews showing best fit superpositions of the backbone (N, C^α, C) atoms of the 30 final SA structures. The view in B is related to that in A by an approximately 90° rotation about the x axis. The three disulfide bridges are also shown in A. Residues 7–131 and 9–129 are shown in A and B, respectively.

torsion angle bounds. These have mean values of 0.076 Å and 0.389°, respectively, in the low-resolution structures of Smith et al. (1992), 0.033 Å and 0.293°, respectively, in the low-resolution structures of Powers et al. (1992b), and 0.0016 Å and 0.068°, respectively, in the current set of high-resolution structures (Table II). Thus, the high-resolution structures display 20–50- and 4–5-fold improvements in agreement with the interproton distance and torsion angle restraints, respectively, relative to the previous low-resolution structures, consistent with the large increase in the number and correctness of the experimental restraints.

Description of the Structure. The secondary structure elements present in IL-4 are summarized in Table III. The overall structure of IL-4 consists of four α-helices arranged in a left-handed helical bundle. A unique characteristic of the IL-4 structure is the orientation of the helices in which adjacent helices are anti-parallel while nonadjacent opposing helices are parallel. This results in two overhand connections in the form of two long loops with some irregular β-strand characteristics. Indeed, part of these two long loops actually forms a short antiparallel β-sheet between residues 32–34 and 110–112. Helix α_A (residues 8–24) leads into a five-residue helical turn (ht$_A$, residues 27–31), followed by a strand (β_A, residues 32–34) that runs in an anti-parallel direction to helix α_A and a loop (residues 35–43) that leads into helix α_B (residue 44–66). Helices α_B and α_C (residues 73–98) are connected by a short loop (residues 67–72) that contains a five-residue helical turn (ht$_B$, residues 67–71). Helix α_C leads into a loop (residues 99–109) and a short strand (β_B, residues

110–112) that runs anti-parallel to α_C and leads directly into the fourth helix, α_D (residues 113–128).

The structure of IL-4 contains three disulfide linkages. The N- and C-termini of the protein are connected by the disulfide bond between Cys 7 and Cys 131, which is ill-defined. The disulfide bridge between Cys 28 and Cys 69 connects the two helical turns, ht$_A$ and ht$_B$. The average C^α–$C^{\alpha'}$ distance between Cys 28 and Cys 69 was only 5.1 ± 0.1 Å. This very short C^α–$C^{\alpha'}$ distance resulted in χ_1(Cys 28), χ_2(Cys 28), χ_3, χ_2'(Cys 69), and χ_1'(Cys 69) angles of –133 ± 4°, 58 ± 2°, 75 ± 7°, –167 ± 6°, and –44 ± 12°, respectively. The disulfide bridge between Cys 50 and Cys 103 connects helix α_B to the loop from residues 99–109. The average C^α–$C^{\alpha'}$ distance between Cys 50 and Cys 103 was 6.9 ± 0.02 Å, indicative of an extended conformation typically observed in disulfides that span the β-barrels in immunoglobulins or short loops, with χ_1(Cys 50), χ_2(Cys 50), χ_3, χ_2'(Cys 103), and χ_1'(Cys 103) angles of 160 ± 7°, –160 ± 6°, –117 ± 4°, –145 ± 1°, and –176 ± 11°, respectively.

The IL-4 molecule is oblong in shape with approximate dimensions of ~41 × ~28 × ~19 Å. This is reflective of the four relatively long α-helices of approximately equal lengths which are packed into the left-handed bundle (Tables III and IV). The angles and axial separations between the long axes of the four anti-parallel helical pairs, α_A–α_C, α_C–α_B, α_B–α_D, and α_D–α_A, are –157° and 11.1 Å, –154° and 10.2 Å, –152° and 7.7 Å, and –148° and 11.8 Å, respectively. The corresponding values between the parallel helical pairs, α_A–α_B and α_C–α_D, are 40° and 14.9 Å and 36° and 15.1 Å,
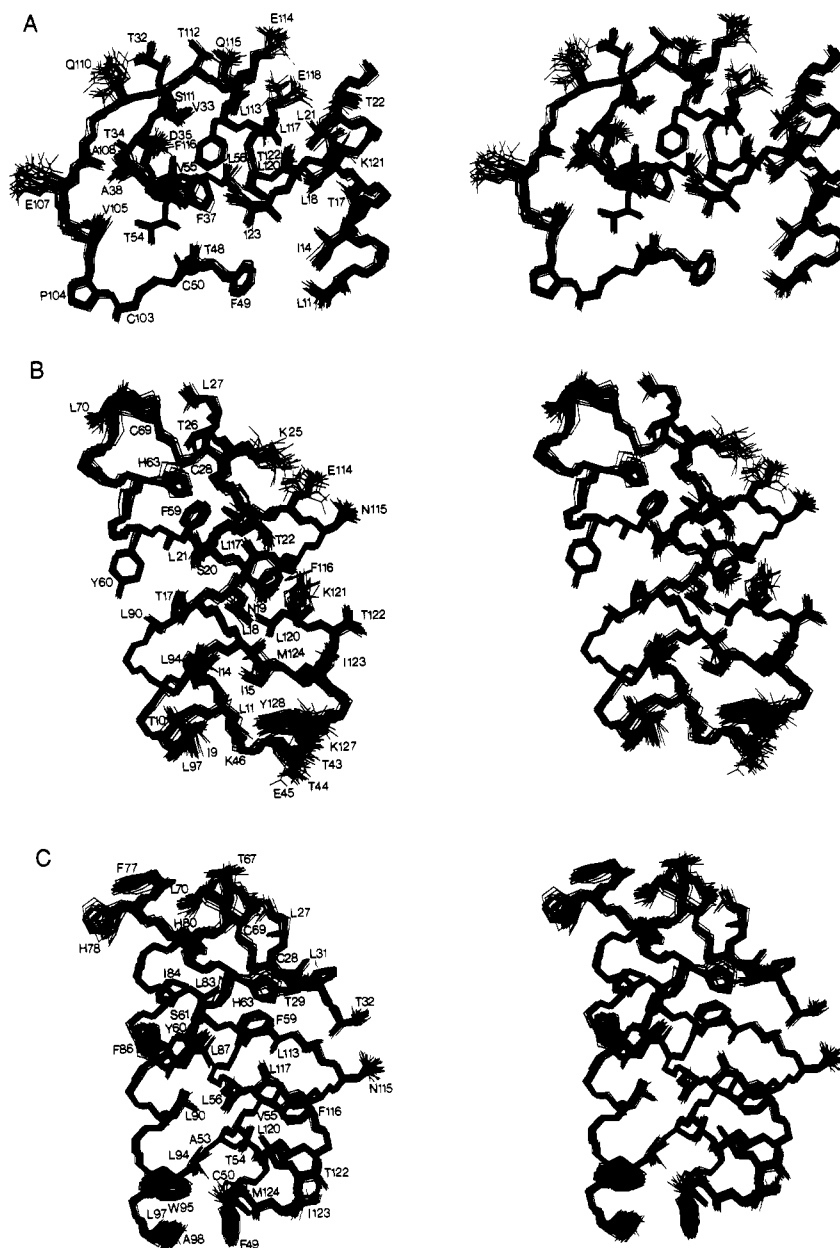
FIGURE 7: Stereoviews showing best fit superpositions of all atoms (excluding hydrogens and backbone carbonyls) of the 30 SA structures for three selected segments of IL-4. Side-chain–side-chain interactions between helices α_A, α_B, and α_D and β-strands β_A and β_B are shown in A, between helices α_A, α_C, and α_D in B, and between helices α_B, α_C, and α_D in C.

respectively. Thus, the angle Ω (Chothia, 1984) between the long axes of adjacent anti-parallel helices, when projected onto their plane of contact, ranges from $+23°$ to $+32°$. In terms of the "ridges into grooves" model of helix packing, this corresponds to class 3-4 packing in which one helix uses $\pm4n$ ridges and the other uses $\pm3n$ ridges (Chothia et al., 1977, 1981) (i.e., the ridges on the helix surface are formed by side chains separated by four and three residues in the sequence, respectively).

The nature of the helix packing is dependent on side-chain–side-chain interactions. The core of the IL-4 protein is entirely hydrophobic. The residues involved in the helix packing are Leu 11, Ile 14, Leu 18, and Leu 21 of helix α_A, Phe 49, Ala 52, Ala 53, Leu 56, Phe 59, and Tyr 60 of helix α_B, Leu 83, Ile 84, Leu 87, Leu 90, Leu 94, and Leu 97 of helix α_C, and Leu 113, Phe 116, Leu 117, Leu 120, Met 124, and Tyr 128 of helix α_D. The interactions of these side chains at the interface of helices α_A, α_B, and α_D, helices α_A, α_C, and α_D, and helices α_B, α_C, and α_D are illustrated in Figure 7A–C,

respectively. In addition, there are a number of hydrophobic interactions between strand β_A and helices α_B and α_D that are illustrated in Figure 7A. Specifically, Val 33 of strand β_A is in contact with Val 55 and Phe 116, Ile 36 is in contact with Ala 52, and Phe 37 is in contact with Ile 123.

It appears from Figure 6A that residues 73–80 in helix α_C extend beyond the helix bundle and are solvent-exposed. The orientation of this segment of helix α_C with respect to the core of the protein, however, is well-defined and is stabilized by numerous hydrophobic side-chain–side-chain interactions involving the helical turns ht_A and ht_B. In particular, Gln 76 is in close proximity to Thr 26 and Leu 27, Phe 77 is in close proximity to Leu 70, Arg 79 is in close proximity to Gln 24 and Thr 26, and His 80 is in close proximity to His 63, Glu 64, Cys 69, and Leu 70 (Figure 7C).

The presence of *potential* hydrogen bonds or salt bridges involving side chains and bound water in the IL-4 structure was ascertained after the final 30 SA structures were calculated. The restrained minimized average structure,
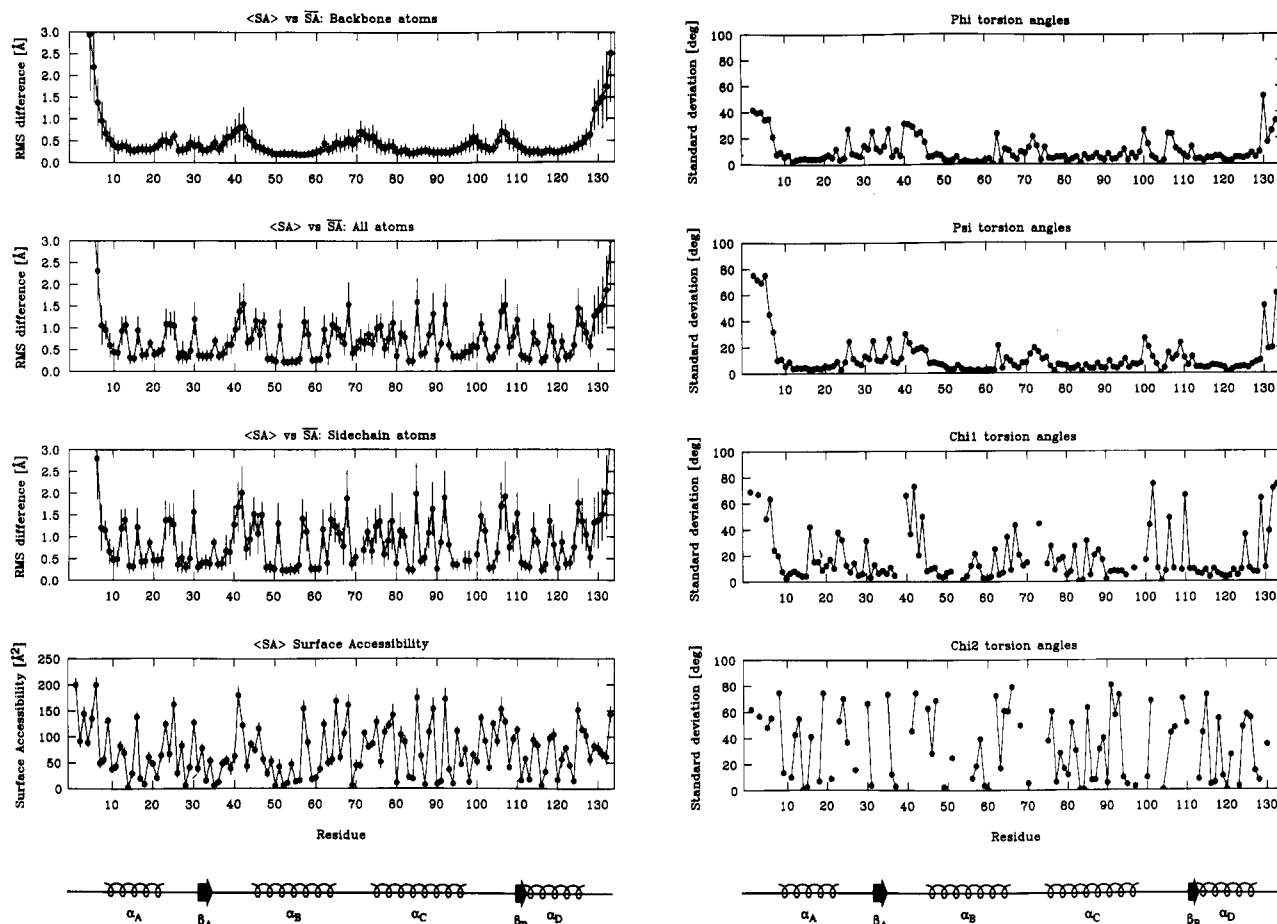
FIGURE 8: Atomic rms distribution of the 30 individual SA structures about the mean structure $\overline{SA}$, for the backbone (N, C$^\alpha$, C, O) atoms, all atoms, and side-chain atoms as a function of residue number, together with the variation in surface accessibility of each residue (left). Standard deviation of the backbone ϕ and ψ and side-chain χ_1 and χ_2 torsion angles for the 30 SA structures as a function of residue number (right). The black circles represent the average values at each residue, and the error bars indicate the standard deviations in these values. The bottom of the figure presents a schematic diagram of the secondary structure of IL-4, with helices shown as helical coils and β-strands shown as arrows.
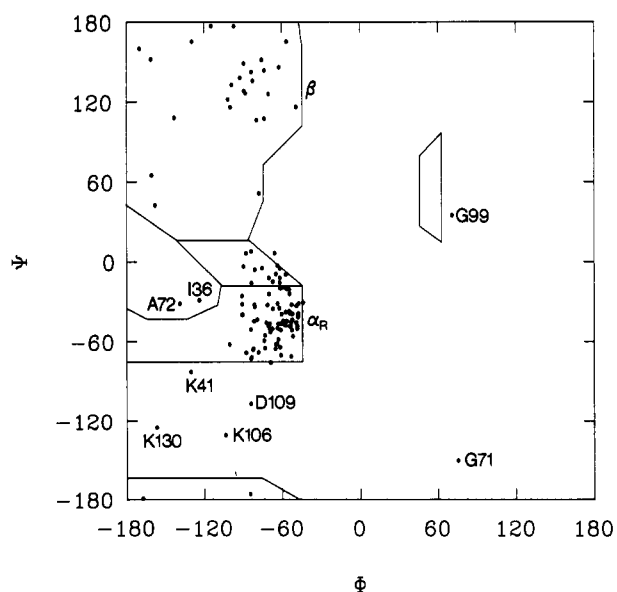

FIGURE 9: Ramachandran ϕ,ψ plot for the restrained minimized mean structure, $(\overline{SA})r$, of IL-4. Non-glycine residues that lie outside the allowed regions of the Ramachandran plot (indicated by the solid lines) and glycine residues lying in the positive ϕ region of the plot are labeled.

$(\overline{SA})r$, of IL-4 with side chains involved in potential hydrogen bonds, salt bridges, and interactions with tightly bound water

Table III: Summary of Secondary Structure Elements Present in the Solution Structure of IL-4, together with a Comparison with Those Present in the Crystal Structures of GM-CSF and HGH

secondary structural elements	IL-4	GM-CSF[a]	HGH[a]
helices			
A	8–24	13–28	9–34
B	44–66	55–64	72–92
C	73–98	68–87	106–128
D	113–128	103–116	148–180
helical turns			
A	27–31	33–36	38–47,[b] 64–70[b]
B	67–71		94–100
β-strands			
A	32–34	39–43	
B	110–112	98–102	

[a] From the X-ray structures of GM-CSF (Diederichs et al., 1991) and HGH (De Vos et al., 1992). [b] These residues comprise two small helices located in the connecting loop between helices A and B (i.e., they are significantly longer than the helical turns present in IL-4 and GM-CSF).

is illustrated in Figure 10. The approximate positions of the two tightly bound water molecules (lifetime > 1 ns) in the average IL-4 structure are indicated by solid spheres, since the exact positioning of the water molecules could not be determined.

The presence of tightly bound water was determined from ROEs between water and side-chain amide groups observed in the 3D ^{15}N-edited ROESY spectrum (Figure 5). Three

Table IV: Interhelical Angles and Axial Separations between Pairs of Helices Comprising the Left-Handed Four-Helix Bundle Observed in the NMR Structure of IL-4, together with a Comparison with Those Found in the X-ray Structures of IL-4, GM-CSF, and HGH[a]

helical pairs[b]	interhelical angle (axial separation, Å)			
	IL-4 (NMR)[c]	IL-4 (X-ray)[d]	GM-CSF[e]	HGH[f]
A–C	–157° (11.1)	–153° (8.8)	–151° (8.6)	–145° (10.7)
A–D	–154° (10.2)	–152° (8.5)	–149° (10.4)	–155° (6.0)
B–C	–152° (7.7)	–151° (7.9)	–167° (7.4)	–157° (8.9)
B–D	–148° (11.8)	–149° (11.9)	–141° (10.0)	–155° (10.1)
A–B	40° (14.9)	41° (14.8)	39° (14.5)	43° (13.9)
C–D	36° (15.1)	41° (12.3)	40° (11.0)	34° (12.5)

[a] The interhelical angles (degrees) between each helical pair is followed by the axial separation (angstroms) in parentheses. [b] The first four helical pairs are anti-parallel, while the last two are parallel. [c] IL-4 (NMR) is the restrained minimized mean NMR structure, (SA)r (see footnote *a* to Table II). [d] IL-4 (X-ray) is the 2.25 Å resolution crystal structure of IL-4 (Wlodawer et al., 1992). [e] From the X-ray structure of GM-CSF (Diederichs et al., 1991). [f] From the X-ray structure of HGH (De Vos et al., 1992).

such ROEs were observed involving the side-chain amide groups of Gln 24, Gln 76, and Gln 82. The close proximity of Gln 24 and Gln 82 in the structure suggests that a single bound water (W1) bridges these two side chains. W1 probably adds additional stability to the C-terminus of helix α_A since Gln 24 is the C-terminal residue of this helix. Further, W1 also increases the packing stability of helix α_A to helix α_B by removing a potentially destabilizing side-chain interaction. The second bound water (W2) is in close proximity to the side-chain amide group of Gln 76. Inspection of the structure strongly suggests that W2 is involved in a network of bridging hydrogen bonds comprising the side-chain amide group of Gln 76 and the backbone carbonyl groups of Gln 76 and Cys 69. Hence, W2 is likely to play an important role in stabilizing the N-terminal end of helix α_C via the water-bridged interaction with Cys 69 in helical turn ht$_B$.

While the interior of IL-4 is highly hydrophobic, the exterior is highly hydrophilic and comprises a high percentage of charged residues (12 Lys, 9 Arg, 8 Glu, and 6 Asp). Analysis of the final SA structures suggests the presence of eight potential hydrogen bonds or salt bridges involving surface side chains. The side chains of some of these residues, in particular Glu 45, Arg 51, Gln 58, Arg 119, Lys 121, and Lys 127, are partially disordered in the ensemble of SA structures, as no additional restraints for the proposed hydrogen bonds or salt bridges were included in the refinement. In each case, however, the poorly defined moiety of the side chain only involves the terminal functional group (i.e., the side-chain carboxylate, guanidinium, or amide) which is not associated with any NOE restraints and is therefore free to rotate about the adjoining bond; the rest of the side chain, on the other hand, is reasonably well-defined (see footnote *k* to Table II). As a result, the side chains of these residues relative to the remainder of the protein are sufficiently well-positioned to permit the presence of potential hydrogen bond or salt bridge interactions to be inferred by manipulation of the functional groups using interactive modeling tools.

Some of the hydrogen bond/salt bridge interactions involve neighboring residues in a helix or helical turn, thereby further contributing to its stability. Examples of this type of interaction include the hydrogen bonds between the hydroxyl group of Thr 29 and the backbone carbonyl of Thr 26 in helical turn ht$_A$, between the hydroxyl group of Thr 48 and the backbone carbonyl of Thr 44 in helix α_B, and between the hydroxyl group of Thr 112 and the side-chain amide group

of Asn 115 in helix α_D. The remaining interactions are clearly involved in stabilizing the packing of the four helices and/or maintaining the tertiary structure of IL-4. Specifically, there are three interhelical interactions: the carbonyl side chain of Asn 19 in helix α_A is hydrogen-bonded to the N$^\varsigma$H$_3^+$ group of Lys 121 in helix α_D; the carboxylate side chain of Glu 45 at the N-terminus of helix α_B is salt-bridged to the N$^\varsigma$H$_3^+$ of Lys 127 at the C-terminus in helix α_D; and the side-chain amide group of Gln 58 in helix α_B is hydrogen-bonded to the hydroxyl group of Thr 24 in helix α_A. Finally, there are two interactions which stabilize the positioning of strand β_A with respect to helices α_B and α_D, namely, the carboxylate side chain of Asp 35 at the end of strand β_A is hydrogen-bonded to the guanidinium group of Arg 119 in helix α_D, and the backbone carbonyl of Ala 39 in the loop connecting helix α_B and strand β_A is hydrogen-bonded to the guanidinium group of Arg 51 in helix α_B. The hydrogen bond/salt bridge involving Asp 35 is of particular interest as it serves to neutralize the negative charge on the completely buried side chain of Asp 35, which has a surface accessibility of only ~6 Å^2.

Comparison of the Solution Structure of IL-4 with the X-ray Structure. Shortly after the publication of our initial low-resolution (second generation) NMR structure of IL-4 (Powers et al., 1992b), two crystal structures of IL-4 were determined: one at 2.25-Å resolution (Wlodawer et al., 1992) and the other at 2.35-Å resolution (Walter et al., 1992a). The superposition of the backbone atoms of the restrained minimized mean, (SA)r, high-resolution NMR structure and the 2.25-Å resolution X-ray structure of Wlodawer et al. (1992) is shown in Figure 11, together with a plot of the backbone atomic rms differences as a function of residue. Clearly the two structures are similar, both in terms of overall topology and alignment of the four-helix bundle, as evidenced by the very good agreement in the calculated interhelical angles (Table III). Nevertheless, there are some significant differences, as evidenced by the relatively large rms differences between the two structures. Thus, excluding residues 1–7 and 130–133 at the N- and C-termini, respectively, the atomic rms difference between the restrained minimized mean NMR structure, (SA)r, and the X-ray structure is 1.37 Å for the backbone atoms and 2.24 Å for all atoms (Table II). When only residues involved in secondary structure are considered, these values drop to 1.04 and 1.94 Å, respectively.

These relatively large rms differences can be attributed to rigid-body displacements of the helices such that the four-helix bundle is more tightly packed in the crystal structure than the NMR structure. In particular, the axial separation for three pairs of helices, α_A–α_C, α_A–α_D, and α_C–α_D, is reduced by approximately 20% from 11.1, 10.2, and 15.1 Å, respectively, in the NMR structure to 8.8, 8.5, and 12.3 Å, respectively, in the crystal structure. This is also accompanied by a decrease in the radius of gyration from 14.7 Å in the NMR structure to 14.2 Å in the crystal structure. The higher degree of compactness of the crystal structure can probably be attributed to the mobility and flexibility of the protein in solution and to crystal packing forces arising from interactions with neighboring protein molecules in the crystal lattice. In this regard it is interesting to note that in the crystal lattice residues 66–76 in the loop connecting helices α_B and α_C are in contact with the N-terminus of helix α_A and the C-terminus of helix α_C of a second molecule and with the C-terminus of helix α_D of a third molecule.

The conformation of the Cys 28–Cys 69 disulfide bridge, which is associated with a very short C$^\alpha$–C$^{\alpha'}$ distance, is the same in the NMR and X-ray structures, the χ angles differing
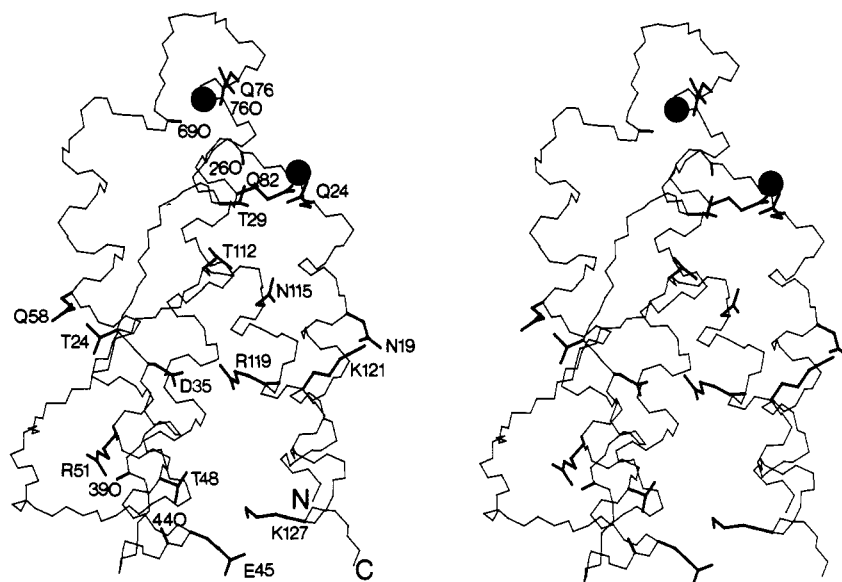
FIGURE 10: Stereoview of the backbone (N, C$^\alpha$, C) atoms of the restrained minimized mean structure, $\overline{(SA)}$r, of IL-4 (residues 9–129), together with side chains or backbone carbonyl groups of residues involved in potential hydrogen bonds and salt bridges. The approximate locations of the two bound water molecules are indicated by the black circles.

on average by no more than 20–25°. The conformation of the Cys 50–Cys 103 disulfide bridge, however, differs significantly between the two structures. Whereas the χ angles in the NMR structure are typical of an extended disulfide bridge conformation (see above), those in the X-ray structure are highly unusual and skewed (Richardson, 1981) with χ_1(Cys 50), χ_2(Cys 50), χ_3, χ_2'(Cys 103), and χ_1'(Cys 103) angles of 169°, –94°, 154°, 114°, and –93°, respectively. Indeed, there do not appear to be any examples of χ_3 angles which does not lie within a ±30° range of either +90° or –90° (Richardson, 1981).

The other major differences between the NMR and crystal structures lie in three loop regions comprising residues 35–43, 67–72, and 99–109, which connect helices α_A and α_B, helices α_B and α_C, and helices α_C and α_D, respectively. Again, mobility in solution and crystal packing are likely to be major contributors to these differences. Thus, for example, residues 40–45 of one molecule lie anti-parallel to residues 40–45 of a second molecule in the crystal lattice with four hydrogen bonds between the two molecules at this location [Ser 40-(CO)–Thr 48′(O$^{\gamma 1}$H), Thr 43(NH)–Asn 42′(O$^\delta$), Thr 44-(NH)–Lys 41′(CO), and Thr 44(NH)–Ser 40′(CO)]. Similarly, the orientation with respect to the core of the protein of the loop comprising residues 67–72 is clearly influenced by crystal packing, as described above. In solution, on the other hand, ^{15}N heteronuclear relaxation measurements indicate that loops comprising residues 35–43 and 99–109 exhibit a significant degree of motion on the picosecond time scale and are characterized by low (0.2–0.6) values for the overall order parameters, S^2 (Redfield et al., 1992).

The significance of the structural differences between the NMR and crystal structures is indicated by the very high values of the NOE and torsion angle restraint energies (Table II) and the large number of interproton distance and torsion angle violations greater than 2 Å and 60°, respectively, exhibited by the X-ray structure (Table V). Many of the larger interproton distance violations are a result of different χ rotamers between the X-ray and NMR structures. A particular example is Trp 95, which has χ_1 and χ_2 angles of 176 ± 5° and –91 ± 4°, respectively, in the NMR structures and –63° and 108°, respectively, in the crystal structure. This

difference is real and is verified by a significant number of NOEs which could only be present in the χ_1,χ_2 = 180°, –90° conformer and by the absence of NOEs which could only be present in the χ_1,χ_2 = –60°,90° conformation.

The χ_1 torsion angles of a number of internal residues in the X-ray structure are significantly skewed from the normal rotamer positions. The distortion of these torsion angles, which may be a reflection of the tighter helix packing in the crystal structure, also results in significant NOE and torsion angle violations, but does not affect the general character of the side-chain–side-chain interactions.

The backbone ϕ and ψ restraint violations seen in the crystal structure are located in the two mobile loop regions (residues 35–43 and 99–109). These violations are probably of little significance since the NMR structure corresponds to an average structure and the crystal structure corresponds to a particular "frozen-out" conformation that is also influenced by crystal packing forces.

It is also interesting to note that, from an energetic viewpoint, the value of the Lennard Jones–van der Waals energy is less negative for the crystal structure (–368 kcal mol^{-1}) than for the NMR structure (–477 kcal mol^{-1}). This may be a reflection of the tighter packing of the helices, resulting in some poor nonbonded contacts. There is no significant difference, however, in the values of the solvation free energy of folding for the solution and crystal structures (Table II).

Comparison of the Solution Structure of IL-4 with the Crystal Structures of Human Growth Hormone and Granulocyte–Macrophage Colony Stimulating Factor. The left-handed four-helix bundle motif with two overhand connections observed in the structure of IL-4 is relatively unique. To our knowledge, it has only been observed in four other proteins, all of which bind to the same superfamily of hematopoietic receptors (Boulay & Paul, 1992): growth hormone (Abdel-Meguid et al., 1987; de Vos et al., 1992), granulocyte-macrophage colony stimulating factor (GM-CSF; Diedrichs et al., 1991; Walter et al., 1992b), interleukin-2 (Bazan, 1992; McKay, 1992), and macrophage colony stimulating factor (Pandit et al., 1992). The coordinates of human growth hormone (HGH) and GM-CSF were kindly provided to us by Drs. A. M. de Vos and A. Kossiakoff and Dr. P. A. Karplus,
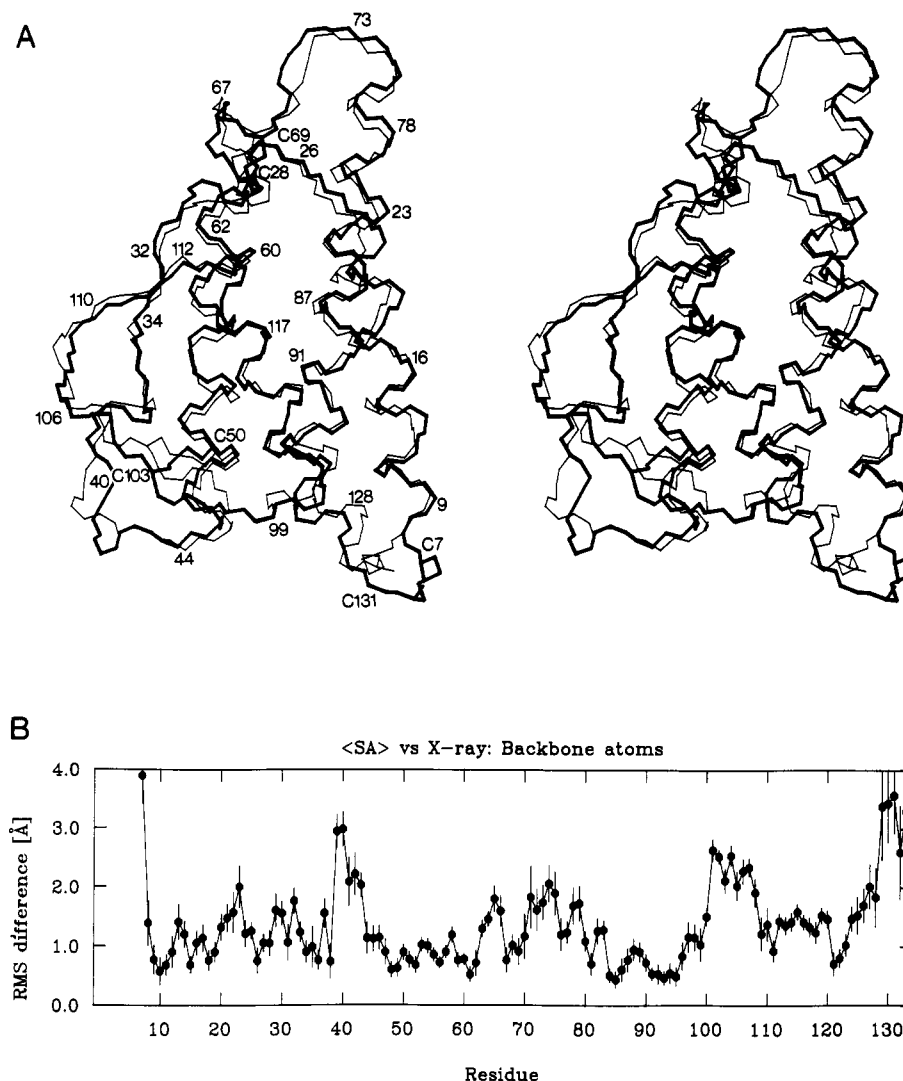
A

B

<SA> vs X−ray: Backbone atoms

RMS difference [Å]

Residue

FIGURE 11: Best fit superposition of the backbone (N, C$^\alpha$, C) atoms of the restrained minimized mean NMR (thick line) structure and the X-ray (thin line) structure of IL-4 for residues 7–131 (A). Backbone (N, C$^\alpha$, C, O) atomic rms difference between the 30 SA structures and the X-ray structure as a function of residue number (B). The black circles represent the average values at each residue and the bars the standard deviations of these values. The X-ray structure is that of Wlodawer et al. (1992).

respectively, and the results of a comparison with the NMR structure of IL-4 are discussed below.

Even though there is no significant overall sequence identity between IL-4, HGH, and GM-CSF, their overall topology is very similar, as illustrated both by the ribbon digrams shown in Figure 12 and by the very similar values for the interhelical angles and axial separation within the four-helix bundle, listed in Table III. There is one significant topological difference, however, between IL-4 and GM-CSF on the one hand and HGH on the other. Namely, in the case of IL-4 and GM-CSF, the N-terminal end of the overhand loop connecting helices α_A and α_B passes behind helix α_D in the view shown in Figure 12, while in the case of HGH it passes in front of helix α_D.

A least-squares match of the C$^\alpha$ coordinates using the program O (Jones & Kjeldgaard, 1990) reveals that 72 residues of IL-4 and GM-CSF and 79 residues of IL-4 and HGH can be superimposed with atomic rms differences of 1.7 and 2 Å, respectively (Table VI). The resulting best fit superpositions are also shown in Figure 12, and the corresponding sequence alignments are given in Figure 13. The extent of sequence identity within these matched regions of structure is small, namely, 25% for IL-4 and GM-CSF and only 10% for IL-4 and HGH.

The principal differences between IL-4, GM-CSF, and HGH reside in the relative lengths of the helices, the nature and lengths of connecting elements, and the number and pattern of disulfide bonds. A comparison of the secondary structure elements present in the three structures is listed in Table III. Inspection of the ribbon drawings shown in Figure 12 indicates that GM-CSF is smaller than IL-4, whereas HGH is larger than IL-4. This is reflected in the lengths of all helices in the three structures. The helices in GM-CSF, IL-4, and HGH range from 10 to 20 residues, 17 to 26 residues, and 21 to 33 residues, respectively, in length. In addition, the relative lengths of the helices in each structure differ. In the case of HGH, helices α_A and α_D are longer than helices α_B and α_C, whereas the reverse is true for IL-4. For GM-CSF, helices α_A and α_C are longer than α_B and α_D. These differences result in a distinct alteration in the surface at the top of the front face in the view shown in Figure 12.

The connecting elements between the various helices also differ in the three structures. IL-4 has two helical turns, one connecting helices α_A and α_B and the other connecting helices α_B and α_C, and a small anti-parallel β-sheet connecting the two loops between helices α_A and α_B and helices α_C and α_D. In GM-CSF, the helical turn between helices α_B and α_C is missing. This is probably due to the fact that this connecting
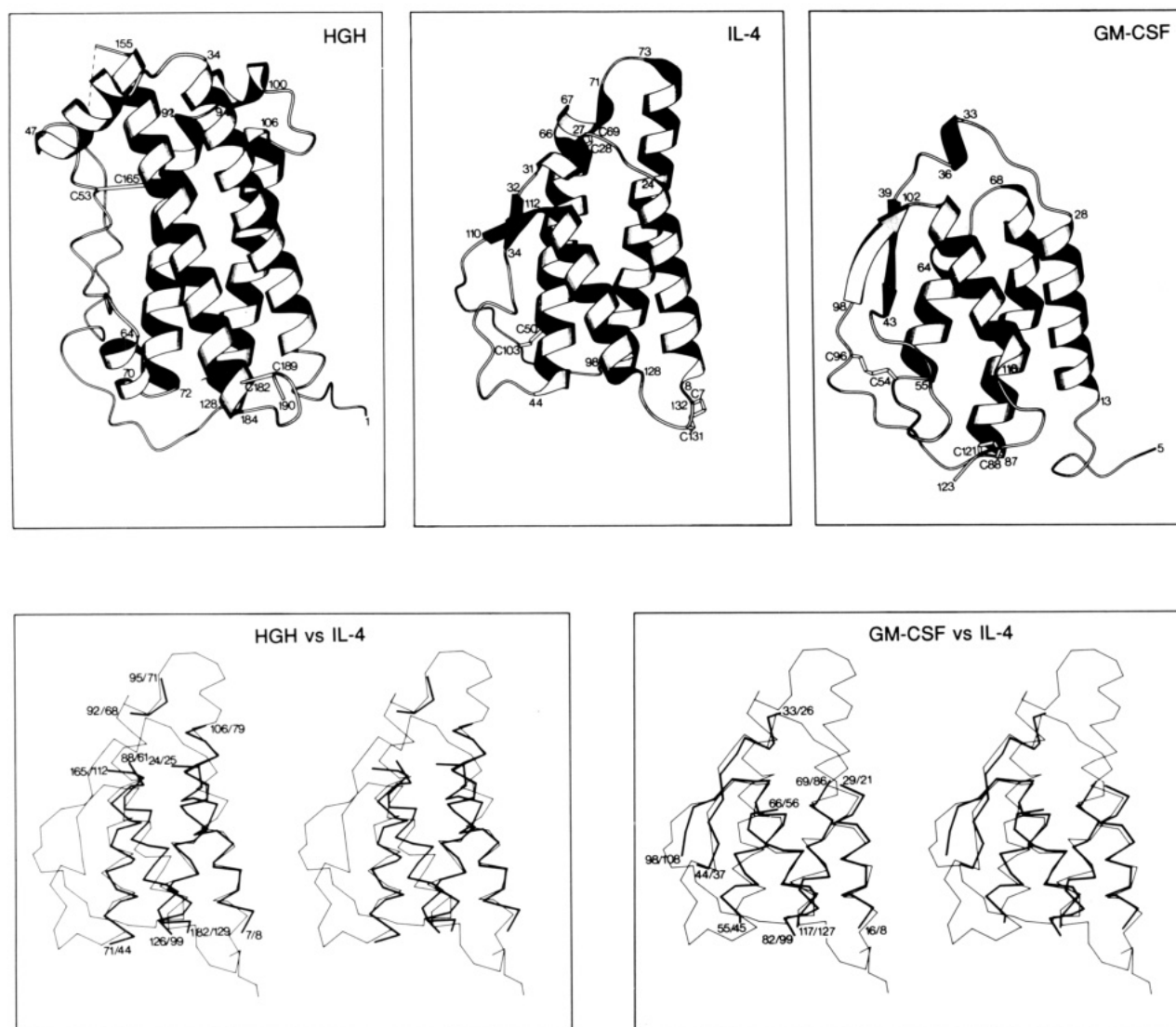
FIGURE 12: Ribbon drawings of the restrained minimized mean NMR structure of IL-4 and the X-ray structures of HGH and GM-CSF (top panels). Residues 7–132 are shown for IL-4, residues 1–190 for HGH, and residues 5–123 for GM-CSF. The three disulfide bridges in IL-4 and the two disulfide bridges in HGH and GM-CSF are labeled along with the beginning and the end of the helical regions. In the bottom panels, best fit superpositions of the C^α atoms of the restrained minimized mean NMR (thin line) structure of IL-4 with the C^α atoms of the matched residues of the X-ray structures (thick lines) of HGH (79 residues) and GM-CSF (72 residues) are shown. The residue numbers at the beginning and the end of each fragment are indicated, the first number corresponding to HGH or GM-CSF and the second to IL-4. The best fit matches for the structural alignment were obtained using the program O (Jones & Kjeldgaard, 1992). The ribbon diagrams were generated with the program Molscript (Kraulis, 1991).

element is significantly shorter in GM-CSF (three residues) than in IL-4 (six residues). Conversely, the anti-parallel β-sheet is two residues longer in GM-CSF than in IL-4. The differences in the connecting elements between IL-4 and HGH are more distinctive. In HGH, the anti-parallel β-sheet is absent and an additional short (seven residue) helix is present between helices α_A and α_B. This additional helix can be formed because the linker between helices α_A and α_B is approximately twice as long as the linker in IL-4 (19 residues compared to 37 residues) and, hence, does not need to adopt an entirely extended conformation to complete the link between the two helices.

In addition, the pattern and number of disulfide linkages differ in the three structures. IL-4 has three disulfide bridges, whereas both HGH and GM-CSF have only two disulfide linkages. The disulfide linkages in GM-CSF connect helix α_B to the loop region between helices α_C and α_D, and the C-terminus to helix α_C. The disulfide linkages in HGH connect helix α_D to the loop region between helices α_A and α_B, and the C-terminus to helix α_D.

Biological Implications. The striking qualitative and quantitative resemblance of the topologies of IL-4, GM-CSF, and HGH illustrated in Figure 12 was unexpected given the very limited amount of overall sequence similarity. One rationale for this observation may be provided by the fact that the receptors for these three proteins belong to the same hematopoietic superfamily. If this interpretation is accurate, then one would expect all three proteins to interact with their cell surface receptor in a similar manner. The crystal structure of the HGH–receptor complex has been determined (de Vos et al., 1992), and it reveals that a single molecule of HGH is bound to two molecules of receptor. This lends support to the hypothesis that dimerization is responsible for signal transduction by the hematopoietic superfamily of receptors (Cunningham et al., 1991; Fuh et al., 1992; Boulay & Paul, 1992). It may therefore be possible to infer details of the interaction of IL-4 with its cognate receptor on the basis of the structural alignment of IL-4 and HGH presented above (Figure 12).

By analogy with the HGH–receptor complex, we therefore propose that there are two distinct sites of interaction on IL-4.

Table V: Number of Violations Exhibited by the X-ray Structure of IL-4 with Respect to the Experimental NMR Interproton Distance and Torsion Angle Restraints[a]

A. Number of Violations in Interproton Distance Restraints					
	0.1–0.3 Å	0.3–0.5 Å	0.5–1.0 Å	1.0–2.0 Å	2.0–5.0 Å	>5.0 Å
all (2617)	74	69	85	89	58	5
interresidue						
sequential ($|i-j| = 1$) (522)	21	15	22	17	7	0
short ($1 < |i-j| \leq 5$) (549)	16	26	22	32	28	3
long ($|i-j| > 5$) (560)	22	13	30	33	23	2
intraresidue (884)	9	11	10	7	0	0
H-bonds (102)	6	4	1	0	0	0

B. Violations in Torsion Angle Restraint			
	10–30°	30–60°	60–120°	>120°
all (356)	18	12	16	12
ϕ (130)	4	0	2	0
ψ (119)	4	4	3	1
χ_1 (73)	6	4	8	4
χ_2 (32)	4	4	3	7
χ_3 (2)	0	0	0	0

[a] The X-ray structure of IL-4 corresponds to that of Wlodawer et al. (1992). The total number of interproton distance and torsion angle restraints in each category is given in parentheses.

The interaction site for the first receptor molecule would involve the surface formed mainly by helix α_D, strand β_A, and the loop connecting strand β_A to helix α_B (bottom left-hand side of Figure 6A and bottom of Figure 6B), while the interaction site for the second receptor molecule would involve the surface formed by helices α_A and α_C (bottom right-hand side of Figure 6A and top right of Figure 6B). The structure-based sequence alignment in Figure 13, which is principally restricted to the helical regions, then permits one to infer potential residues of IL-4 involved in contacting the two receptor molecules by direct analogy with the HGH system. Residues comprising the first site in HGH are His 18 in helix α_A and Arg 167, Lys 168, Asp 171, Thr 175, and Arg 178 in helix α_D, which correspond to Asn 19, Glu 114, Asn 115, Glu 118, Thr 122, and Arg 125, respectively, in IL-4. In addition to these residues, we would also predict the potential involvement in IL-4 of Lys 121, Glu 126, and Tyr 128. Residues constituting the second site in HGH are Asn 12, Leu 15, Arg 16, and Arg 19 in helix α_A and Asp 116 and Glu 119 in helix α_C, which correspond to Glu 13, Lys 16, Thr 17, Ser 20, Arg 89, and Arg 92, respectively, in IL-4. Other likely residues in this site that could potentially make contact with the IL-4 receptor are Thr 10 in helix α_A and Asn 93 in helix α_C.

Three mutational studies are of interest in the light of the above prediction. First, analysis of a series of human–mouse GM-CSF chimera has indicated that residues 21–31 and 78–94, which correspond to the second interaction site described above, are important for recognition (Kaushansky et al., 1989). Second, site-specific mutagenesis data on GM-CSF have implicated a critical role for Glu 21 (equivalent to Glu 13 in IL-4; cf. Figure 13) in high-affinity binding to the β-receptor chain (Lopez et al., 1992). Third, a mutation in the first interaction site of Tyr 128 to Asp in IL-4 results in the generation of a competitive IL-4 antagonist which still binds to the receptor with high affinity ($\sim$60% of wild type), but no longer possesses any proliferative activity for T-cells (Kruse et al., 1992).

It could be argued that the effect of the Tyr 128 → Asp mutation in IL-4 arises from the removal of an important hydrophobic interaction with the receptor molecule. This is

unlikely since the aromatic ring of Tyr 128 has only limited surface accessibility ($\sim$50 Å^2) and only the hydroxyl group is directly solvent-exposed (cf. Figures 7C and 8). If the interaction of the hydroxyl group with the receptor molecule were crucial for IL-4 activity, one would speculate that adding the negatively charged Asp residue might actually *increase* the stability of the interaction or, at the least, have no effect. In fact, replacement of Tyr 128 by a positively charged Lys resulted in a mutant with a higher level of activity than the Tyr 128 → Asp mutant (Kruse et al., 1992). In addition, complete removal of the hydroxyl group in the Tyr 128 → Phe mutant resulted in a protein for which complete activity and binding affinity were preserved (Kruse et al., 1992). This indicates that the effect of the Tyr 128 → Asp mutation is probably not the result of a direct loss of a specific interaction with the receptor molecule, but in all likelihood arises from a local loss of the structural integrity of IL-4, a very likely occurrence given the fact that the side chain at position 128 resides on the interior face of the helix.

Tyr 128 is the C-terminal residue of helix α_D, which is part of the first proposed binding site. Any local unwinding or disruption of helix α_D could be severe enough to eliminate this binding site. There is a significant amount of evidence that suggests that electrostatic interactions are important in α-helix formation (Shoemaker et al., 1987). These results suggest that appropriately charged groups at the N- and C-termini of a helix can interact favorably with the positive and negative poles, respectively, of the α-helix macrodipole, thereby stabilizing the helix. Therefore, by analogy, the mutation of Tyr 128 to the negatively charged Asp residue probably destabilizes the α_D helix because of its unfavorable interaction with the negative pole of the α-helix macrodipole. Indeed, the probability of finding an Asp residue at the C-terminus of an α-helix in native proteins is very low (Shoemaker et al., 1987). This also explains why the Tyr 128 → Lys mutation has a higher relative activity than the Tyr 128 → Asp mutation, since the positively charged Lys would interact favorably with the negative pole of the helix macrodipole. Even though the Tyr 128 → Lys mutation probably stabilizes the formation of helix α_D, the mutant is significantly less active than native IL-4, presumably because of a conformational effect on receptor binding due to the introduction of a positive charge at this location. The Tyr 128 → Asp mutation is obviously only severe enough to eliminate one receptor binding site, consistent with the 60% decrease in receptor binding affinity. [Note that the stoichiometry of receptor binding for the wild-type and mutant proteins was not established (Kruse et al., 1992)]. The other mutations at position 128 (Phe, His, Asn, Lys, Gly) all have similar receptor binding affinity to wild-type IL-4, but exhibit varying degrees of reduced biological efficacy. This suggests that the effects of these various Tyr 128 mutations only result in local structural perturbations affecting a single receptor binding site. Hence, the observation that the Tyr 128 → Asp mutation eliminates IL-4 efficacy and acts as an antagonist is consistent with the view that signal transduction in the IL-4 system involves multiple binding sites on IL-4, possibly causing receptor dimerization. Thus, the antagonist properties of the Tyr 128 → Asp mutant appear to arise from the loss of one binding site and the concomitant prevention of receptor dimerization.

The availability of the high-resolution solution structure of IL-4 presented in this article will permit the design and interpretation of future mutational studies aimed at probing structure–function relationships and delineating the receptor binding sites in more detail. In addition, this structure and

```
              10        15        20        25              30      35              45        50        55      60
IL-4    D I T L Q E I I K T L N S L T E Q K     T L C T E L T V T D I F     T E K E T F C R A A T V L R Q F Y S

                 20        25                        35      40                55        60        65
GM-CSF  V N A I Q E A R R L L N L S             A A E M N E T V E V I S       L Q T R L E L Y K Q G L

              10        15        20                                              75        80        85
HGH     S R L F D N A M L R A H R L H Q L A                                 S N L E L L R I S L L L I Q S W L E
               Δ       Δ Δ   *   Δ


              70        80        85        90        95              110       115       120       125
IL-4    R C L G     R H K Q L I R F L K R L D R N L W G L A G         A D Q S T L E N F L E R L K T I M R E K Y S

                          70        75        80                          100       105       110       115
GM-CSF                S L T K L K G P L T M M A S                     T Q I I T F E S F K E M L K D F L L V I

              95        110       115       120       125                 165       170       175       180
HGH     F L R S     S D S N V Y D L L K D L E E G I Q T L M G         C F R K D M D K V E T F L R I V Q C
                                    Δ       Δ                             * *     *         *       *
```
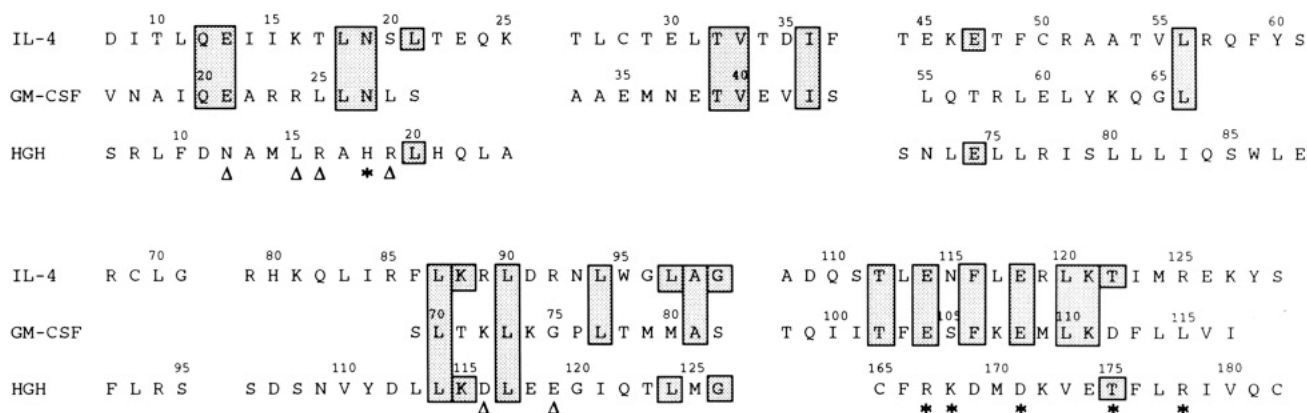
FIGURE 13: Sequence alignment of IL-4, HGH, and GM-CSF based on the structural superposition shown in Figure 12. The asterisks and triangles indicate the residues of HGH that interact with the first and second receptor molecules, respectively, in the X-ray structure of the HGH–receptor complex (de Vos et al., 1992). Sequence identities are indicated by the shaded boxes.

Table VI: C^α Atomic rms Differences between the NMR Structure of IL-4 and the X-ray Structures of IL-4, GM-CSF, and HGH

structure	C^α atomic rms difference (Å)[a,b]		
	IL-4 (X-ray)	GM-CSF	HGH
IL-4 (NMR)	1.37 (122)	1.72 (72)	1.98 (79)
IL-4 (X-ray)		1.86 (72)	1.93 (79)
GM-CSF			1.93 (61)

[a] The structural alignment and best fit superpositions were carried out using the program O (Jones & Kjeldgard, 1992). The notation of the structures is the same as that in Table IV. The C^α rms difference between the IL-4 NMR and X-ray structures is restricted to residues 8–129, as the N- and C-termini are disordered in solution and the X-ray structure starts at residue 5. The C^α rms difference between the IL-4 and GM-CSF structures was based on the structural alignment of residues 8–21, 26–37, 45–56, 89–99, and 108–127 of IL-4 on residues 16–29, 33–44, 55–66, 69–82, and 98–117 of GM-CSF, respectively. The C^α rms difference between the IL-4 and HGH structures was based on the structural alignment of residues 8–25, 44–61, 68–71, 79–99, and 112–129 of IL-4 on residues 7–24, 71–88, 92–95, 106–126, and 165–182 of HGH, respectively. The C^α rms difference between GM-CSF and HGH structures was based on the structural alignment of residues 14–29, 55–66, 69–85, and 102–117 of GM-CSF on residues 5–20, 72–83, 113–129, and 165–180 of HGH, respectively. [b] The numbers in parentheses indicate the number of matched residues used in the calculation of the C^α rms differences.

the associated NMR spectroscopic data will provide the basis for future studies aimed at determining the three-dimensional structure of the IL-4–receptor complex in solution.

SUPPLEMENTARY MATERIAL AVAILABLE

One table giving a complete list of ^1H, ^{13}C, and ^{15}N resonance assignments for IL-4, including stereospecific assignments of β-methylene protons and methyl groups of Leu and Val (6 pages). Ordering information is given on any current masthead page. In addition, the coordinates of the 30 final simulated annealing structures of IL-4, together with the coordinates of the restrained minimized mean structure, (SA)r, and the complete list of experimental NMR restraints, have been deposited in the Brookhaven Protein Data Bank.

REFERENCES

Abdel-Meguid, S. S., Shiel, H.-S., Smith, W. W., Dayringer, H. E., Violand, B. N., & Bentle, L. A. (1987) Proc. Natl. Acad. Sci. U.S.A. 84, 6434–6437.

Archer, S. J., Ikura, M., Sporn, M. B., Torchia, D. A., & Bax, A. (1991) J. Magn. Reson. 95, 636–641.

Bax, A., & Davis, D. G. (1985) J. Magn. Reson. 63, 207–213.

Bax, A., & Pochapsky, S. S. (1992) J. Magn. Reson. 99, 638–643.

Bax, A., Sklenar, V., & Summers, M. F. (1986) J. Magn. Reson. 70, 327–331.

Bax, A., Ikura, M., Kay, L. E., Torchia, D. A., & Tschudin, R. (1990) J. Magn. Reson. 86, 304–318.

Bax, A., Max, D., & Zax, D. (1992) J. Am. Chem. Soc. 114, 6924–6925.

Bazan, J. F. (1992) Science 257, 410–412.

Bodenhausen, G., & Ruben, D. J. (1980) Chem. Phys. Lett. 69, 185–189.

Bothner-By, A. A., Stephens, R. L., Lee, J. T., Warren, C. D., & Jeanloz, R. W. (1984) J. Am. Chem. Soc. 106, 811–813.

Boulay, L.-L., & Paul, W. E. (1992) J. Biol. Chem. 267, 20525–20528.

Brooks, B. R., Bruccoleri, R. E., Olafson, B. D., States, D. J., Swaminathan, S., & Karplus, M. (1983) J. Comput. Chem. 4, 187–217.

Brünger, A. T. (1992) XPLOR Version 3.0 Manual, Yale University, New Haven, CT.

Brünger, A. T., Clore, G. M., Gronenborn, A. M., & Karplus, M. (1986) Proc. Natl. Acad. Sci. U.S.A. 83, 3801–3805.

Chiche, L., Gregoret, L. M., Cohen, F. E., & Kollman, P. A. (1990) Proc. Natl. Acad. Sci. U.S.A. 87, 3240–3243.

Chothia, C. (1984) Annu. Rev. Biochem. 53, 537–572.

Chothia, C., Levitt, M., & Richardson, J. S. (1977) Proc. Natl. Acad. Sci. U.S.A. 74, 4310–4314.

Chothia, C., Levitt, M., & Richardson, J. S. (1981) J. Mol. Biol. 145, 215–250.

Clore, G. M., & Gronenborn, A. M. (1991a) Annu. Rev. Biophys. Biophys. Chem. 20, 29–63.

Clore, G. M., & Gronenborn, A. M. (1991b) Science 252, 1390–1399.

Clore, G. M., & Gronenborn, A. M. (1992) J. Mol. Biol. 223, 853–856.

Clore, G. M., Nilges, M., Sukumaran, D. K., Brünger, A. T., Karplus, M., & Gronenborn, A. M. (1986) EMBO J. 5, 2729–2735.

Clore, G. M., Gronenborn, A. M., Nilges, M., & Ryan, C. A. (1987) Biochemistry 26, 8012–8013.

Clore, G. M., Bax, A., Wingfield, P. T., & Gronenborn, A. M. (1990a) Biochemistry 29, 5671–5676.

Clore, G. M., Appella, E., Yamada, M., Matsushima, K., & Gronenborn, A. M. (1990b) *Biochemistry 29*, 1689–1696.

Clore, G. M., Driscoll, P. C., Wingfield, P. T., & Gronenborn, A. M. (1990c) *J. Mol. Biol. 214*, 811–817.

Clore, G. M., Bax, A., & Gronenborn, A. M. (1991a) *J. Biomol. NMR 1*, 13–22.

Clore, G. M., Kay, L. E., Bax, A., & Gronenborn, A. M. (1991b) *Biochemistry 30*, 12–18.

Clore, G. M., Wingfield, P. T., & Gronenborn, A. M. (1991c) *Biochemistry 30*, 2315–2323.

Clore, G. M., Robien, M. A., & Gronenborn, A. M. (1993) *J. Mol. Biol. 231*, 82–102.

Cunningham, B. C., Ultsch, M., De Vos, A. M., Mulkerrin, M. G., Clauser, K. R., & Wells, J. A. (1991) *Science 254*, 821–825.

Curtis, B. M., Presnell, S. R., Srinivasan, S., Sassenfeld, H., Klinke, R., Jeffery, E., Cosman, D., March, C. J., & Cohen, F. E. (1991) *Proteins: Struct. Funct. Genet. 11*, 111–119.

De Vos, A. M., Ultsch, M., & Kossiakoff, A. A. (1992) *Science 255*, 306–312.

Diederichs, K., Boone, T., & Karplus, P. A. (1991) *Science 254*, 1779–1782.

Eisenberg, D., & McLachlan, A. D. (1986) *Nature 319*, 199–203.

Finkelman, F. D., Holmes, J., Katonn, I. M., Urban, J. F., Beckmann, M. P., Peik, L. S., Hooley, K. A., Coffman, R. L., Momman, T. R., & Paul, W. E. (1990) *Annu. Rev. Immunol. 8*, 303–333.

Forman-Kay, J. D., Gronenborn, A. M., Kay, L. E., Wingfield, P. T., & Clore, G. M. (1990) *Biochemistry 29*, 1566–1572.

Forman-Kay, J. D., Clore, G. M., Wingfield, P. T., & Gronenborn, A. M. (1991a) *Biochemistry 30*, 2685–2698.

Forman-Kay, J. D., Gronenborn, A. M., Wingfield, P. T., & Clore, G. M. (1991b) *J. Mol. Biol. 220*, 209–216.

Fuh, G., Cunningham, B. C., Fukunaga, R., Nagata, S., Goeddel, D. V., & Wells, J. A. (1992) *Science 256*, 1677–1680.

Garrett, D. S., Powers, R., Gronenborn, A. M., & Clore, G. M. (1991) *J. Magn. Reson. 95*, 214–220.

Garrett, D. S., Powers, R., March, C. J., Frieden, E. A., Clore, G. M., & Gronenborn, A. M. (1992) *Biochemistry 31*, 4347–4353.

Golumbek, P. T., Lazenby, A. J., Levitzky, H. I., Jaffee, L. M., Karasuyama, H., Baker, M., & Pardoll, D. M. (1991) *Science 254*, 713–716.

Gronenborn, A. M., Filpula, D. R., Essig, N. Z., Achari, A., Whitlow, M., Wingfield, P. T., & Clore, G. M. (1991) *Science 253*, 657–661.

Grzesiek, S., Ikura, M., Clore, G. M., Gronenborn, A. M., & Bax, A. (1992) *J. Magn. Reson. 96*, 215–222.

Ikura, M., Kay, L. E., Tschudin, R., & Bax, A. (1990a) *J. Magn. Reson. 86*, 204–209.

Ikura, M., Bax, A., Clore, G. M., & Gronenborn, A. M. (1990b) *J. Am. Chem. Soc. 112*, 9020–9022.

Jones, T. A. (1978) *J. Appl. Crystallogr. 11*, 268–272.

Jones, T. A., & Kjeldgard, M. (1992) *Manual for O, version 5.7.1*, Uppsala University, Uppsala, Sweden.

Kaushanksy, K., Shoemaker, S. G., Alfaro, S., & Brown, C. (1989) *Proc. Natl. Acad. Sci. U.S.A. 82*, 1213–1217.

Kay, L. E., & Bax, A. (1989) *J. Magn. Reson. 86*, 110–126.

Kay, L. E., Marion, D., & Bax, A. (1989) *J. Magn. Reson. 84*, 72–84.

Kay, L. E., Clore, G. M., Bax, A., & Gronenborn, A. M. (1990) *Science 249*, 411–414.

Kraulis, P. J. (1991) *J. Appl. Crystallogr. 24*, 946–950.

Kraulis, P. J., Clore, G. M., Nilges, M., Jones, T. A., Petterson, G., Knowles, J., & Gronenborn, A. M. (1989) *Biochemistry 28*, 7241–7257.

Kruse, N., Tony, H.-P., & Sebald, W. (1992) *EMBO J. 11*, 3237–3244.

Kühn, R., Rajewsky, K., & Muller, W. (1991) *Science 254*, 707–710.

Kuszewski, J., Nilges, M., & Brunger, A. T. (1992) *J. Biomol. NMR 2*, 33–56.

Lopez, A. F., Shannon, M. F., Herces, T., Nicola, N. A., Cambareri, B., Dottore, M., Layton, M. J., Eglinton, J., & Vada, M. A. (1992) *EMBO J. 11*, 909–916.

Marion, D., Ikura, M., Tschudin, R., & Bax, A. (1989a) *J. Magn. Reson. 85*, 393–399.

Marion, D., Driscoll, P. C., Kay, L. E., Wingfield, P. T., Bax, A., Gronenborn, A. M., & Clore, G. M. (1989b) *Biochemistry 28*, 6150–6156.

McGregor, M. J., Islam, S. A., & Sternberg, M. J. E. (1987) *J. Mol. Biol. 198*, 295–310.

McKay, D. B. (1992) *Science 257*, 412–413.

Messerle, B. A., Wilder, G., Otting, G., Weber, C., & Wuthrich, K. (1989) *J. Magn. Reson. 85*, 608–613.

Nilges, M., Clore, G. M., & Gronenborn, A. M. (1988a) *FEBS Lett. 229*, 317–324.

Nilges, M., Gronenborn, A. M., Brünger, A. T., & Clore, G. M. (1988b) *Protein Eng. 2*, 27–38.

Nilges, M., Clore, G. M., & Gronenborn, A. M. (1988c) *FEBS Lett. 239*, 129–136.

Nilges, M., Clore, G. M., & Gronenborn, A. M. (1990) *Biopolymers 29*, 813–822.

Norwood, T. J., Boyd, J., Heritage, J. E., Soffe, N., & Campbell, I. D. (1990) *J. Magn. Reson. 87*, 488–510.

Omichinski, J. G., Clore, G. M., Appella, E., Sakaguchi, K., & Gronenborn, A. M. (1990) *Biochemistry 29*, 9324–9334.

Otting, G., & Wüthrich, K. (1989) *J. Am. Chem. Soc. 111*, 1871–1875.

Pandit, J., Bohm, A., Jancarik, J., Halenbeck, R., Koths, K., & Kim, S.-H. (19920 *Science 258*, 1358–1362.

Paul, W. E. (1991) *Blood 77*, 1859–1870.

Paul, W. E., & Ohara, J. (1987) *Annu. Rev. Immunol. 5*, 429–460.

Ponder, J. W., & Richards, F. M. (1987) *J. Mol. Biol. 193*, 775–791.

Powers, R., Gronenborn, A. M., Clore, G. M., & Bax, A. (1991) *J. Magn. Reson. 94*, 209–213.

Powers, R., Garrett, D. S., March, C. J., Frieden, E. A., Gronenborn, A. M., & Clore, G. M. (1992a) *Biochemistry 31*, 4334–4346.

Powers, R., Garrett, D. S., March, C. J., Frieden, E. A., Gronenborn, A. M., & Clore, G. M. (1992b) *Science 256*, 1673–1677.

Refield, C., Boyd, J., Smith, L. J., Smith, R. A. G., & Dobson, C. M. (1992) *Biochemistry 31*, 10431–10437.

Richardson, J. (1981) *Adv. Protein Chem. 34*, 167–339.

Shoemaker, K. R., Kim, P. S., York, E. J., Stewart, J. M., & Baldwin, R. L. (1987) *Nature 326*, 563–567.

Smith, L. J., Redfield, C., Boyd, J., Lawrence, G. M. P., Edwards, R. G., Smith, R. A. G., & Dobson, C. M. (1992) *J. Mol. Biol. 224*, 899–904.

Tepper, R. I., Pattengale, P. K., & Leder, P. (1989) *Cell 57*, 503–510.

Tepper, R. I., Coffman, R. L., & Leder, P. (1992) *Science 257*, 548–551.

Vuister, G. W., Delaglio, F., & Bax, A. (1992) *J. Am. Chem. Soc. 114*, 9674–9675.

Vuister, G. W., Clore, G. M., Gronenborn, A. M., Powers, R., Garrett, D. S., Tschudin, R., & Bax, A. (1993) *J. Magn. Reson., Ser. B 101*, 210–213.

Wagner, G., Braun, W., Havel, T. F., Schaumann, T., Go, N., & Wüthrich, K. (1987) *J. Mol. Biol. 196*, 611–639.

Walter, M. R., Cook, W. J., Zhao, B. G., Cameron, R. P., Ealick, S. E., Water, R. L., Reichert, P., Nagabhushan, T. L., Trotta, P. P., & Bugg, C. E. (1992a) *J. Biol. Chem. 29*, 20371–20376.

Walter, M. R., Cook, W. J., Ealick, S. E., Nagabhushan, T. L., Trotta, P., & Bugg, C. E. (1992b) *J. Mol. Biol. 224*, 1075–1085.

Williamson, M. P., Havel, T. F., & Wüthrich, K. (1985) *J. Mol. Biol. 182*, 295–315.

Wlodawer, A., Pavlovsky, A., & Gustchina (1992) *FEBS Lett. 309*, 59–64.

Wüthrich, K., Billetter, M., & Braun, W. (1983) *J. Mol. Biol. 169*, 949–961.

Yokota, T., Arai, N., de Vries, J., Spits, H., Banchereau, J., Zlotnik, A., Rennick, D., Howard, M., Takebe, Y., Miyatake, S., Lee, F., & Arai, K. (1988) *Immunol. Rev. 103*, 137–187.

Zhu, G., & Bax, A. (1990) *J. Magn. Reson. 90*, 405–410.

Zuiderweg, E. R. P., & Fesik, S. W. (1989) *Biochemistry 28*, 2387–2391.

Zuiderweg, E. R. P., Boelens, R., & Kaptein, R. (1985) *Biopolymers 24*, 601–611.

Zuiderweg, E. R. P., McIntosh, L. P., Dahlquist, F. W., & Fesik, S. W. (1990) *J. Magn. Reson. 86*, 210–216.

Zuiderweg, E. R. P., Petros, A. M., Fesik, S. W., & Olejniczak, E. T. (1991) *J. Am. Chem. Soc. 113*, 370–371.